

MICROMECHANICS OF LOCALIZED FRACTURE PHENOMENA IN INELASTIC SOLIDS GENERATED BY IMPACT-LOADED ADIABATIC PROCESSES

P. P e r z y n a

**Institute of Fundamental Technological Research
Polish Academy of Sciences**

Pawińskiego 5B, 02-106 Warszawa, Poland
e-mail: pperzyna@ippt.gov.pl

The main objective of the present paper is to discuss very efficient procedure of the numerical investigation of localized fracture in inelastic solids generated by impact-loaded adiabatic processes. Particular attention is focused on the proper description of a ductile mode of fracture propagating along the shear band for high impact velocities. This procedure of investigation is based on utilization the finite difference method for regularized thermo-elasto-viscoplastic constitutive model of damaged material. A general constitutive model of thermo-elasto-viscoplastic damaged polycrystalline solids with a finite set of internal state variables is used. The set of internal state variables consists of two scalars, namely equivalent inelastic deformation and volume fraction porosity. The equivalent inelastic deformation can describe the dissipation effects generated by viscoplastic flow phenomena and the volume fraction porosity takes into account the microdamage evolution effects. The relaxation time is used as a regularization parameter. Fracture criterion based on the evolution of microdamage is assumed.

As a numerical example we consider dynamic shear band propagation and localized fracture in an asymmetrically impact-loaded prenotched thin plate. The impact loading is simulated by a velocity boundary condition which are the results of dynamic contact problem. The separation of the projectile from the specimen, resulting from wave reflections within the projectile and the specimen, occurs in the phenomenon.

A thin shear band region of finite width which undergoes significant deformation and temperature rise has been determined. Its evolution until occurrence of final fracture has been simulated. Shear band advance, microdamage and the development of the temperature field as a function of time have been determined. Qualitative comparison of numerical results with experimental observation data has been presented. The numerical results obtained have proven the usefulness of the thermo-elasto-viscoplastic theory in the investigation of dynamic shear band propagations and localized fracture.

Key words: localized fracture, finite difference method, thermo-elasto-viscoplasticity, microdamage.

1. PROLOGUE

In technological processes fracture can occur as a result of an adiabatic shear band localization generally attributed to a plastic instability generated by in-

trinsic microdamage mechanisms within a material and thermal softening during plastic deformation.

Recent experimental observations have shown that the shear band procreates in a region of a body deformed where the resistance to plastic deformation is lower and the predisposition for localized shear band formation is higher. In the explanation of the fracture phenomenon along shear band regions very important role has the microdamage process which consists of the nucleation, growth and coalescence of microcracks. It has been found experimentally that in dynamic processes the shear band regions behave differently than adjacent zones. Within the shear band region the deformation process is characterized by very large strains (shear band strains over 100%) and very high strain rates (10^4 – 10^6 s⁻¹). The strain rate sensitivity of a material becomes very important feature of the shear band region and the microdamage process is intensified. The mechanism of final failure is a simple propagation of a macrocrack along the damaged material within the shear band region.

The main objective of the present paper is to discuss very efficient procedure of the numerical investigation of localized fracture in inelastic solids generated by impact-loaded adiabatic processes. Particular attention is focused on the proper description of a ductile mode of fracture propagating along the shear band for high impact velocities.

This procedure of investigation is based on utilization the finite difference method for regularized thermo-elasto-viscoplastic constitutive model of damaged material.

In this paper emphasis is laid on experimental and physical foundations as well as on mathematical constitutive modelling for the description of polycrystalline solids in modern technological processes. Our aim is twofold. First, particular attention will be focused on the fundamental mathematical analysis of the initial-boundary value problem (the evolution problem) and its proper numerical solution. We shall discuss the well-posedness of the evolution problem, its discretization in space and time, its approximated scheme, and its consistency, stability and convergence. Second, very important part of the discussion will also concern the physical aspects of the dispersion waves in considered numerical example. It will be proved that dispersive waves have a great influence on the results concerning the evolution of adiabatic shear bands as well as the propagation of the macrocrack path. It will be shown that cooperative phenomena generated by the interaction of dispersive and dissipative effects influence the final results concerning localized fracture of the considered specimen.

A general constitutive model of thermo-elasto-viscoplastic damaged polycrystalline solids with a finite set of internal state variables is used. The set of internal state variables consists of two scalars, namely equivalent inelastic deformation and volume fraction porosity. The equivalent inelastic deformation can

describe the dissipation effects generated by viscoplastic flow phenomena and the volume fraction porosity takes into account the microdamage evolution effects. The relaxation time is used as a regularization parameter. Fracture criterion based on the evolution of microdamage is assumed cf. PERZYNA [37–39, 42–44].

The identification procedure for the material functions and constants involved in the constitutive equations is developed basing on the experimental observations of adiabatic shear bands in an AISI 4340 steel presented by CHAKRABARTI and SPRETNAK [2].

We idealize the initial-boundary value problem investigated experimentally by CHAKRABARTI and SPRETNAK [2] by assuming the velocity driven process for a thin steel (AISI 4340) plate.

Base on the best curve fitting of the experimental results obtained by CHAKRABARTI and SPRETNAK [2] for the stress-strain relation the identification of the material constants has been done. The investigation of the stability and convergence of the numerical method based on the finite difference discretization has been presented, cf. DORNOWSKI and PERZYNA [11].

As a numerical example let us consider dynamic shear band propagation and localized fracture in an asymmetrically impact-loaded prenotched thin plate, cf. DORNOWSKI and PERZYNA [13]. The plate is made of an AISI 4340 steel. A notch (250 μm wide) is further extended by 2 mm and is situated unsymmetrically on the edge. The constant velocity $V_0 = 38$ m/s is imposed for projectile. The projectile comes into contact with the specimen over the width of 50 mm.

The impact loading is simulated by a velocity boundary condition which are the results of dynamic contact problem. The velocity imposed in specimen in front of projectile increases during the process. The separation of the projectile from the specimen, resulting from wave reflections within the projectile and the specimen, occurs in the phenomenon. All surface areas have traction free boundary conditions except where the velocity boundary condition is applied. We idealize the initial boundary value problem observed experimentally in GUDURU, ROSAKIS and RAVICHANDRAN [21], by assuming the velocity boundary condition and different material of the specimen. The discretization parameters are assumed in such a way, to solve the problem of mesomechanics properly. The dimension of the accepted mesh is of order 20 μm . A thin shear band region of finite width which undergoes significant deformation and temperature rise has been determined. Its evolution until occurrence of final fracture has been simulated.

Shear band advance as a function of time, the evolution of the Mises stress, equivalent plastic deformation, temperature, the microdamage and the crack path in the fracture region have been determined. Very important result is obtained for the evolution of temperature. The distribution of temperature along

shear band is nonuniform, cf. also GLEMA, ŁODYGOWSKI and PERZYNA [20]. This result is in agreement with the experimental observations presented by GUDURU, ROSAKIS and RAVICHANDRAN [21]. They observed that the temperature distribution along the shear band is highly nonuniform, with discrete regions of high temperature, that look like “hot spots”. The evolution of the microdamage and the crack path is very irregular and it widens steadily. It seems that in some places of the crack we can expect the branching effect as it has been observed by GUDURU, ROSAKIS and RAVICHANDRAN [21]. Qualitative comparison of numerical results with experimental observation data has been presented. The numerical results obtained have proven the usefulness of the thermo-elasto-viscoplastic theory in the numerical investigation of dynamic shear band propagation and localized fracture.

2. PHYSICAL AND EXPERIMENTAL MOTIVATION

2.1. Analysis of meso- and micro-mechanical problems

In modern technology we observe recently very important application of metals, ceramics and polymers at meso- and micro-scales. Micromachines are in this size range clearly will be of increasing technological significance. Processes that control the mechanical integrity of microelectronic devices take also place on this size scale, cf. NEEDLEMEN [31] and HUTCHINSON [24].

It is considerable experimental evidence that plastic flow and particularly localization of plastic deformation and localized fracture phenomena in crystalline solids are inherently size dependent over meso- and micro-scales. It is generally accepted that: “smaller is stronger” or “smaller is harder”.

Plastic behaviour at micro-scale range can not be characterized by conventional plasticity theories because they incorporate no material length scale and predict no size effect.

In recent years a variety of theoretical frameworks is emerging to describe inelastic deformation at the meso- and micro-scales. Four such frameworks (constitutive structures), each involving a length scale, are as follows: (i) discrete dislocation plasticity; (ii) nonlocal plasticity; (iii) the coupling of matter diffusion and deformation; (iv) elasto-viscoplasticity.

The meso- and micro-mechanical problems pose also numerical challenges. Computations on smaller size scale require smaller time steps. Since size dependent phenomena come into play when there are gradients of deformation and stress, hence numerical methods are usually needed to obtain solutions. Finite strains and rotations have to be taken into consideration.

At the meso- and micro-scale problems the dominant numerical methods are the finite element and finite difference methods.

It is noteworthy to add that the meso- and micro-scale continuum mechanics is in an early stage of development, both in terms of the theoretical framework as well as the computational methods.

In our consideration we shall use the thermo-elasto-viscoplasticity as a constitutive model of the material and apply the finite difference method in numerical computations.

2.2. Experimental investigation of the initiation and propagation of shear bands

GUDURU, ROSAKIS and RAVICHANDRAN [21] presented an experimental investigation of the initiation and propagation characteristics of dynamic shear band in C300 maraging steel. An elastic discharge machining (EDM) notch (260 μm wide) was further extended by 2 mm by fatigue loading, cf. Fig. 1.

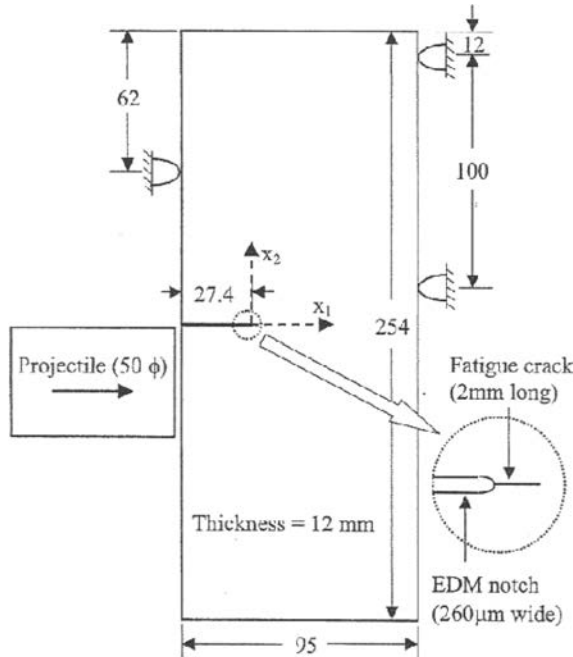


FIG. 1. Specimen geometry and impact arrangement. The projectile is 127 mm long. All dimensions shown are in millimeters (after GUDURU, ROSAKIS and RAVICHANDRAN [21]).

In experimental investigation of GUDURU, ROSAKIS and RAVICHANDRAN [21], two diagnostic techniques were used to observe the crack tip, the propagating shear band and the temperature field evolution during the initiation and propagation of the shear band. On one side of the specimen, the optical technique of coherent gradient sensing (CGS) in reflection was used to monitor the evo-

lution of the stress intensity factors as a function of time. On the other side of specimen, a newly developed full-field, high-speed infrared (IR) imaging system was employed to measure the evolving, 2-D temperature field, cf. Fig. 2. They measure the advance of the shear band and its velocity in five different experiments, cf. Fig. 3 and 4. The shear band velocity can be seen to be highly

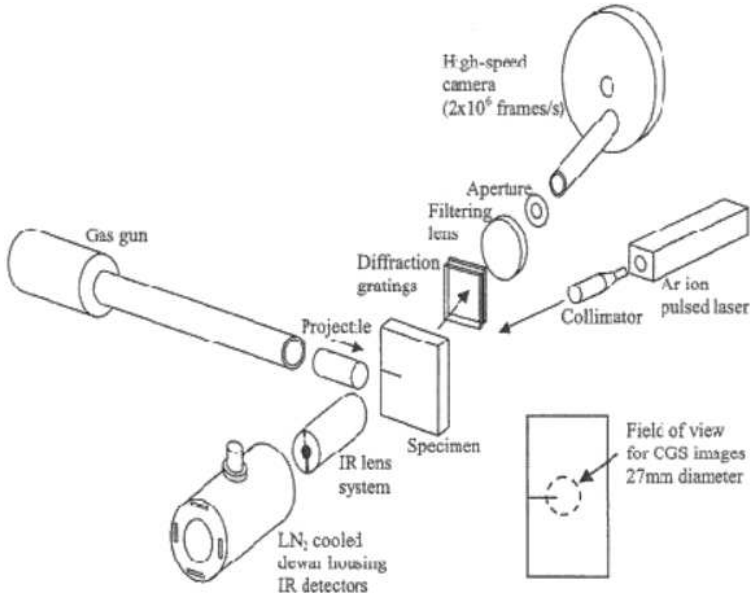


FIG. 2. Schematic illustration of the experimental setup. The CGS setup measures the out plane displacement gradients on the rear side of the specimen. Simultaneous thermal imaging is accomplished using the IR camera on the facing side of the specimen (after GUDURU, ROSAKIS and RAVICHANDRAN [21]).

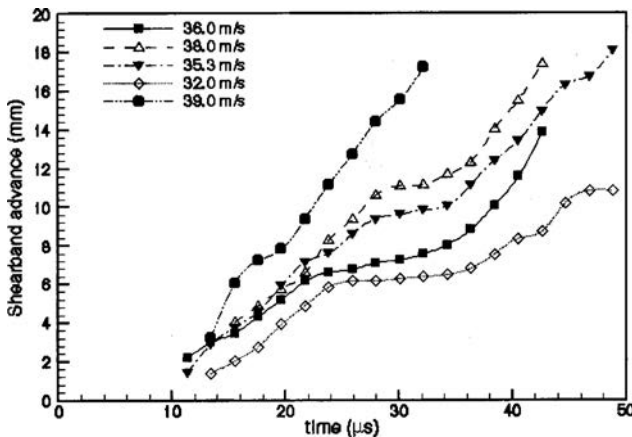


FIG. 3. Shear band advance as a function of time (after GUDURU, ROSAKIS and RAVICHANDRAN [21]).

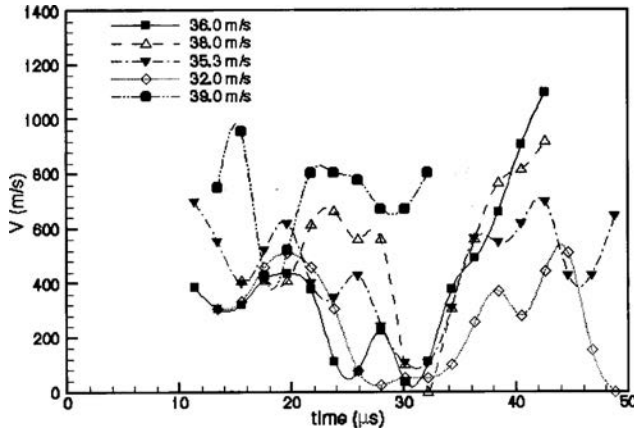


FIG. 4. Shear band velocity as a function of time (after GUDURU, ROSAKIS and RAVICHANDRAN [21]).

transient and a function of the impact speed. In all but one experiment, the band arrests momentarily at about 30 μs , before accelerating to high speeds. The maximum shear band velocity observed here is about 1100 m/s, cf. also ZHOU *et al.* [57, 58].

2.3. Fracture phenomena along localized shear bands

Fractured specimens were examined using an optical microscope to study the features of the shear bands such as its width, trajectory, the fracture surface, etc. The shear band is revealed as a white stripe. The thickness of the band is about 40 μm , cf. Fig. 5. A scanning electron microscope (SEM) image of the specimen surface that failed by shear band propagation, shows elongated voids, with sheared edges that are characteristic of such a failure mode, cf. Fig. 6. The presence of voids reveals the development of triaxiality tensile stress state that led to void growth and eventual fracture.

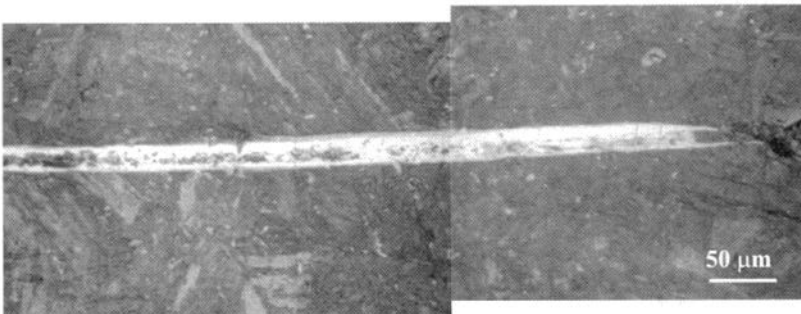


FIG. 5. An optical micrograph of an arrested shear band (after GUDURU, ROSAKIS and RAVICHANDRAN [21]).

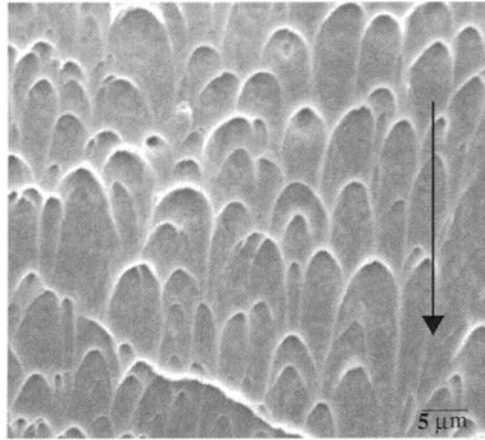


FIG. 6. An SEM image of the fracture surface that failed by shear banding. Arrow shows the crack propagation direction (after GUDURU, ROSAKIS and RAVICHANDRAN [21]).

2.4. Temperature measurement

GUDURU, ROSAKIS and RAVICHANDRAN [21] (cf. also GUDURU *et al.* [22]) performed also broad experimental observations of the temperature field evolution during the initiation and propagation of the shear band. One of their objectives of imaging the temperature field was to visualize the development of the plastic zone at the tip of the initial crack and to observe its evolution, through further localization, into a shear band. The IR camera was focussed at the tip of the fatigue crack as illustrated on the left-hand side of Fig. 7. The impact

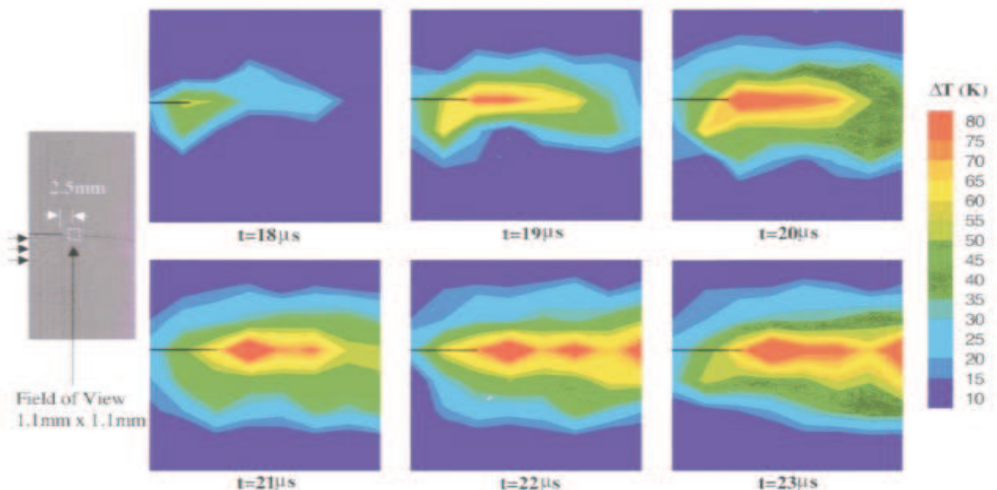


FIG. 7. A sequence of thermal images showing the transition of crack tip plastic zone into a shear band (after GUDURU, ROSAKIS and RAVICHANDRAN [21]).

speed was 35 m/s. They show a sequence of thermal images revealing the development of the temperature field as a function of time. Starting at about 21 μs , the central hot region extends to the right, as indicated by the contour lines, signifying the process of shear localization. The measured highest temperature rise within the plastic zone when this happened was at least 80 K, cf. Fig. 7.

Let us now focus our attention on the temperature field associated with the tip of a propagating shear band. The gradual nature of temperature rise at the front end of shear band supports the notion of a very diffuse shear band tip, as opposed to a crack tip which carries a strong singularity in the field quantities.

As the shear band propagates, the material within the band progressively accumulates large plastic shear strains within short times and the temperature can quickly reach very high value. Of special interest in the investigation of GUDURU, ROSAKIS and RAVICHANDRAN [21] has been the temperature distribution along a well-defined shear band. They have been consistently observed, in all experiments where a propagating shear band was imaged, that the temperature distribution along the band is highly non-uniform, with discrete regions of high temperature, that look like “hot spots”. These hot spots are also seen to translate along the length of the band.

2.5. Possible shear band branching

GUDURU, ROSAKIS and RAVICHANDRAN [21] discussed also the possibility of shear band branching. Figure 8 shows their three micrographs that confirm previous observation about the possibility of shear band branching mode by

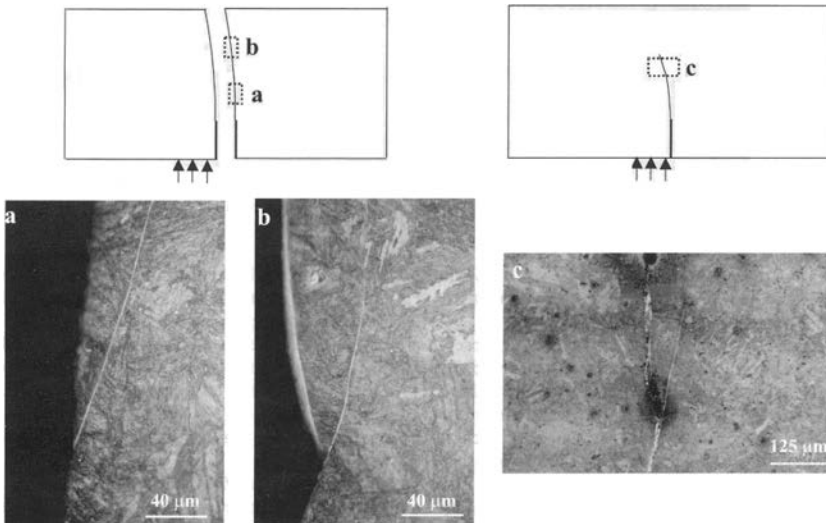


FIG. 8. Optical micrographs of possible shear band bifurcation (after GUDURU, ROSAKIS and RAVICHANDRAN [21]).

MEYERS [30]. In the first two, the left edges are the failure paths, caused by a propagating shear band. The third image is taken from an arrested shear band. The branching behaviour is clearly seen in all three cases. They added that currently there is no theoretical framework to explain such a phenomenon and they stressed that this interesting observation requires further investigation to understand the conditions under which such a bifurcation can take place.

3. THERMO-ELASTO-VISCOPLASTIC MODEL OF A MATERIAL

3.1. Basic assumptions and definitions

Let us assume that a continuum body is an open bounded set $\mathcal{B} \subset \mathbb{R}^3$, and let $\phi : \mathcal{B} \rightarrow \mathcal{S}$ be a C^1 configuration of \mathcal{B} in \mathcal{S} . The tangent of ϕ is denoted $\mathbf{F} = T\phi$ and is called the deformation gradient of ϕ .

Let $\{X^A\}$ and $\{x^a\}$ denote coordinate systems on \mathcal{B} and \mathcal{S} respectively. Then we refer to $\mathcal{B} \subset \mathbb{R}^3$ as the reference configuration of a continuum body with particles $X \in \mathcal{B}$ and to $\mathcal{S} = \phi(\mathcal{B})$ as the current configuration with points $\mathbf{x} \in \mathcal{S}$. The matrix $\mathbf{F}(\mathbf{X}, t) = \partial\phi(\mathbf{X}, t)/\partial\mathbf{X}$ with respect to the coordinate bases $\mathbf{E}_A(\mathbf{X})$ and $\mathbf{e}_a(\mathbf{x})$ is given by

$$(3.1) \quad F_A^a(\mathbf{X}, t) = \frac{\partial\phi^a}{\partial X^A}(\mathbf{X}, t),$$

where a mapping $\mathbf{x} = \phi(\mathbf{X}, t)$ represents a motion of a body \mathcal{B} .

We consider the local multiplicative decomposition

$$(3.2) \quad \mathbf{F} = \mathbf{F}^e \cdot \mathbf{F}^p,$$

where $(\mathbf{F}^e)^{-1}$ is the deformation gradient that releases elastically the stress on the neighbourhood $\phi(\mathcal{N}(\mathbf{X}))$ in the current configuration.

Let us define the total and elastic Finger deformation tensors

$$(3.3) \quad \mathbf{b} = \mathbf{F} \cdot \mathbf{F}^T, \quad \mathbf{b}^e = \mathbf{F}^e \cdot \mathbf{F}^{eT},$$

respectively, and the Eulerian strain tensors as follows

$$(3.4) \quad \mathbf{e} = \frac{1}{2}(\mathbf{g} - \mathbf{b}^{-1}), \quad \mathbf{e}^e = \frac{1}{2}(\mathbf{g} - \mathbf{b}^{e-1}),$$

where \mathbf{g} denotes the metric tensor in the current configuration.

By definition¹⁾

$$(3.5) \quad \mathbf{e}^p = \mathbf{e} - \mathbf{e}^e = \frac{1}{2}(\mathbf{b}^{e-1} - \mathbf{b}^{-1})$$

we introduce the plastic Eulerian strain tensor.

¹⁾For precise definition of the finite elasto-plastic deformation see PERZYNA [41].

To define objective rates for vectors and tensors we use the Lie derivative²⁾. Let us define the Lie derivative of a spatial tensor field \mathbf{t} with respect to the velocity field \mathbf{v} as

$$(3.6) \quad L_{\mathbf{v}}\mathbf{t} = \phi_* \frac{\partial}{\partial t}(\phi^*\mathbf{t}),$$

where ϕ^* and ϕ_* denote the pull-back and push-forward operations, respectively.

The rate of deformation tensor is defined as follows

$$(3.7) \quad \mathbf{d}^b = L_{\mathbf{v}}\mathbf{e}^b = \frac{1}{2}L_{\mathbf{v}}\mathbf{g} = \frac{1}{2}(g_{ac}v^c|_b + g_{cb}v^c|_a)\mathbf{e}^a \otimes \mathbf{e}^b,$$

where the symbol $|_b$ denotes the index lowering operator and \otimes the tensor product,

$$(3.8) \quad v^a|_b = \frac{\partial v^a}{\partial x^b} + \gamma_{bc}^a v^c,$$

and γ_{bc}^a denotes the Christoffel symbol for the general coordinate systems $\{x^a\}$. The components of the spin $\boldsymbol{\omega}$ are given by

$$(3.9) \quad \omega_{ab} = \frac{1}{2}(g_{ac}v^c|_b - g_{cb}v^c|_a) = \frac{1}{2}\left(\frac{\partial v_a}{\partial x^b} - \frac{\partial v_b}{\partial x^a}\right).$$

Similarly

$$(3.10) \quad \mathbf{d}^{e^b} = L_{\mathbf{v}}\mathbf{e}^{e^b}, \quad \mathbf{d}^{p^b} = L_{\mathbf{v}}\mathbf{e}^{p^b},$$

and

$$(3.11) \quad \mathbf{d} = \mathbf{d}^e + \mathbf{d}^p.$$

Let $\boldsymbol{\tau}$ denote the Kirchhoff stress tensor related to the Cauchy stress tensor $\boldsymbol{\sigma}$ by

$$(3.12) \quad \boldsymbol{\tau} = J\boldsymbol{\sigma} = \frac{\rho_{\text{Ref}}}{\rho}\boldsymbol{\sigma},$$

where the Jacobian J is the determinant of the linear transformation $\mathbf{F}(\mathbf{X}, t) = (\partial/\partial X)\phi(\mathbf{X}, t)$, $\rho_{\text{Ref}}(\mathbf{X})$ and $\rho(\mathbf{x}, t)$ denote the mass density in the reference and current configuration, respectively.

The Lie derivative of the Kirchhoff stress tensor $\boldsymbol{\tau} \in \mathbf{T}^2(\mathcal{S})$ (elements of $\mathbf{T}^2(\mathcal{S})$ are called tensors on \mathcal{S} , contravariant of order 2) gives

$$(3.13) \quad L_{\mathbf{v}}\boldsymbol{\tau} = \phi_* \frac{\partial}{\partial t}(\phi^*\boldsymbol{\tau}) = \left\{ \mathbf{F} \cdot \frac{\partial}{\partial t}[\mathbf{F}^{-1} \cdot (\boldsymbol{\tau} \circ \phi) \cdot \mathbf{F}^{-1T}] \cdot \mathbf{F}^T \right\} \circ \phi^{-1} \\ = \dot{\boldsymbol{\tau}} - (\mathbf{d} + \boldsymbol{\omega}) \cdot \boldsymbol{\tau} - \boldsymbol{\tau} \cdot (\mathbf{d} + \boldsymbol{\omega})^T,$$

²⁾The algebraic and dynamic interpretations of the Lie derivative have been presented by ABRAHAM *et al.* [1], cf. also MARSDEN and HUGHES [29].

where \circ denotes the composition of mappings. In the coordinate system (3.13) reads

$$(3.14) \quad (\mathbf{L}_v \boldsymbol{\tau})^{ab} = F_A^a \frac{\partial}{\partial t} \left(F_c^{-1A} \tau^{cd} F_d^{-1B} \right) F_B^b \\ = \frac{\partial \tau^{ab}}{\partial t} + \frac{\partial \tau^{ab}}{\partial x^c} v^c - \tau^{cb} \frac{\partial v^a}{\partial x^c} - \tau^{ac} \frac{\partial v^b}{\partial x^c}.$$

Equation (3.14) defines the Oldroyd rate of the Kirchhoff stress tensor $\boldsymbol{\tau}$ (cf. OLDROYD [33]).

3.2. Constitutive postulates

Let us assume that: (i) conservation of mass, (ii) balance of momentum, (iii) balance of moment of momentum, (iv) balance of energy, (v) entropy production inequality hold.

We introduce the four fundamental postulates:

- (i) Existence of the free energy function. It is assumed that the free energy function is given by

$$(3.15) \quad \psi = \widehat{\psi}(\mathbf{e}, \mathbf{F}, \vartheta; \boldsymbol{\mu}),$$

where \mathbf{e} denotes the Eulerian strain tensor, \mathbf{F} is deformation gradient, ϑ temperature and $\boldsymbol{\mu}$ denotes a set of the internal state variables.

To extend the domain of the description of the material properties and particularly to take into consideration different dissipation effects we have to introduce the internal state variables represented by the vector $\boldsymbol{\mu}$.

- (ii) Axiom of objectivity (spatial covariance). The constitutive structure should be invariant with respect to any diffeomorphism (any motion) $\boldsymbol{\xi} : \mathcal{S} \rightarrow \mathcal{S}$ (cf. MARSDEN and HUGHES [29]). Assuming that $\boldsymbol{\xi} : \mathcal{S} \rightarrow \mathcal{S}$ is a regular, orientation preserving map transforming \mathbf{x} into \mathbf{x}' and $T\boldsymbol{\xi}$ is an isometry from $T_{\mathbf{x}}\mathcal{S}$ to $T_{\mathbf{x}'}\mathcal{S}$, we obtain the axiom of material frame indifference (cf. TRUESDELL and NOLL [54]).
- (iii) The axiom of the entropy production. For any regular motion of a body \mathcal{B} the constitutive functions are assumed to satisfy the reduced dissipation inequality

$$(3.16) \quad \frac{1}{\rho_{\text{Ref}}} \boldsymbol{\tau} : \mathbf{d} - (\eta \dot{\vartheta} + \dot{\psi}) - \frac{1}{\rho \vartheta} \mathbf{q} \cdot \text{grad} \vartheta \geq 0,$$

where ρ_{Ref} and ρ denote the mass density in the reference and actual configuration, respectively, $\boldsymbol{\tau}$ is the Kirchhoff stress tensor, \mathbf{d} the rate of deformation, η is the specific (per unit mass) entropy, and \mathbf{q} denotes the heat

flow vector field. MARSDEN and HUGHES [29] proved that the reduced dissipation inequality (3.16) is equivalent to the entropy production inequality first introduced by COLEMAN and NOLL [5] in the form of the Clausius–Duhem inequality. In fact the Clausius–Duhem inequality gives a statement of the second law of thermodynamics within the framework of mechanics of continuous media, cf. DUSZEK and PERZYNA [14], and PERZYNA [42].

- (iv) The evolution equation for the internal state variable vector $\boldsymbol{\mu}$ is assumed in the form as follows

$$(3.17) \quad L_{\mathbf{v}}\boldsymbol{\mu} = \widehat{\mathbf{m}}(\mathbf{e}, \mathbf{F}, \vartheta, \boldsymbol{\mu}),$$

where the evolution function $\widehat{\mathbf{m}}$ has to be determined based on careful physical interpretation of a set of the internal state variables and analysis of available experimental observations.

The determination of the evolution function $\widehat{\mathbf{m}}$ (in practice a finite set of the evolution functions) appears to be the main problem of the modern constitutive modelling.

The main objective is to develop the rate type constitutive structure for an elastic-viscoplastic material in which the effects of the plastic non-normality, micro-damaged mechanism and thermomechanical coupling are taken into consideration. To do this it is sufficient to assume a finite set of the internal state variables. For our practical purposes it is sufficient to assume that the internal state vector $\boldsymbol{\mu}$ has the form

$$(3.18) \quad \boldsymbol{\mu} = (\epsilon^p, \xi),$$

where ϵ^p is the equivalent viscoplastic deformation, i.e.

$$(3.19) \quad \epsilon^p = \int_0^t \left(\frac{2}{3} \mathbf{d}^p : \mathbf{d}^p \right)^{1/2} dt,$$

and ξ is volume fraction porosity and takes account for micro-damaged effects.

Let us introduce the plastic potential function $f = f(J_1, J_2, \vartheta, \boldsymbol{\mu})$, where J_1, J_2 denote the first two invariants of the Kirchhoff stress tensor $\boldsymbol{\tau}$.

Let us postulate the evolution equations as follows

$$(3.20) \quad \mathbf{d}^p = \Lambda \mathbf{P}, \quad \dot{\xi} = \Xi,$$

where for elasto-viscoplastic model of a material we assume (cf. PERZYNA [34–36, 41])

$$(3.21) \quad \Lambda = \frac{1}{T_m} \left\langle \Phi \left(\frac{f}{\kappa} - 1 \right) \right\rangle,$$

T_m denotes the relaxation time for mechanical disturbances, the isotropic work-hardening-softening function κ is

$$(3.22) \quad \kappa = \widehat{\kappa}(\epsilon^p, \vartheta, \xi),$$

Φ is the empirical overstress function, the bracket $\langle \cdot \rangle$ defines the ramp function,

$$(3.23) \quad \mathbf{P} = \frac{\partial f}{\partial \boldsymbol{\tau}} \Big|_{\xi = \text{const}} \left(\left\| \frac{\partial f}{\partial \boldsymbol{\tau}} \right\| \right)^{-1},$$

Ξ denotes the evolution function which has to be determined.

3.3. Intrinsic micro-damage mechanisms

To take into consideration experimentally observed time dependent effects it is advantageous to use the proposition of the description of the intrinsic micro-damage process presented by PERZYNA [38, 39] and DUSZEK–PERZYNA and PERZYNA [15].

Let us assume that the intrinsic micro-damage process consists of the nucleation and growth mechanisms³⁾.

Physical considerations (cf. CURRAN *et al.* [7] and PERZYNA [38, 39]) have shown that the nucleation of microvoids in dynamic loading processes which are characterized by very short time duration is governed by the thermally-activated mechanism. Based on this heuristic suggestion and taking into account the influence of the stress triaxiality on the nucleation mechanism we postulate for rate dependent plastic flow⁴⁾

$$(3.24) \quad \left(\dot{\xi} \right)_{\text{nucl}} = \frac{1}{T_m} h^*(\xi, \vartheta) \left[\exp \frac{m^*(\vartheta) | I_n - \tau_n(\xi, \vartheta, \epsilon^p) |}{k\vartheta} - 1 \right],$$

where k denotes the Boltzmann constant, $h^*(\xi, \vartheta)$ represents a void nucleation material function which is introduced to take account of the effect of microvoid interaction, $m^*(\vartheta)$ is a temperature dependent coefficient, $\tau_n(\xi, \vartheta, \epsilon^p)$ is the porosity, temperature and equivalent plastic strain dependent threshold stress for microvoid nucleation,

$$(3.25) \quad I_n = a_1 J_1 + a_2 \sqrt{J_2'} + a_3 (J_3')^{1/3}$$

³⁾Experimental observation results (cf. SHOCKEY *et al.* [49]) have shown that coalescence mechanism can be treated as nucleation and growth process on a smaller scale. This conjecture simplifies very much the description of the intrinsic micro-damage process by taking account only of the nucleation and growth mechanisms.

⁴⁾An analysis of the experimental observations for cycle fatigue damage mechanics at high temperature of metals performed by SIDEY and COFFIN [50] suggests that the intrinsic micro-damage process does very much depend on the strain rate effects, the wave shape effects as well as on the stress triaxiality.

defines the stress intensity invariant for nucleation, a_i ($i = 1, 2, 3$) are the material constants, J_1 denotes the first invariant of the Kirchhoff stress tensor $\boldsymbol{\tau}$, J_2' and J_3' are the second and third invariants of the stress deviator $\boldsymbol{\tau}'$.

For the growth mechanism we postulate (cf. JOHNSON [26]; PERZYNA [38, 39]; PERZYNA and DRABIK [45] and DORNOWSKI and PERZYNA [10–12])

$$(3.26) \quad \left(\dot{\xi} \right)_{\text{grow}} = \frac{1}{T_m} \frac{g^*(\xi, \vartheta)}{\kappa_0} [I_g - \tau_{eq}(\xi, \vartheta, \epsilon^p)],$$

where $T_m \kappa_0$ denotes the dynamic viscosity of a material, $g^*(\xi, \vartheta)$ represents a void growth material function and takes account for void interaction, $\tau_{eq}(\xi, \vartheta, \epsilon^p)$ is the porosity, temperature and equivalent plastic strain dependent void growth threshold stress,

$$(3.27) \quad I_g = b_1 J_1 + b_2 \sqrt{J_2'} + b_3 (J_3')^{1/3},$$

defines the stress intensity invariant for growth and b_i ($i = 1, 2, 3$) are the material constants.

Finally the evolution equation for the porosity ξ has the form

$$(3.28) \quad \dot{\xi} = \frac{h^*(\xi, \vartheta)}{T_m} \left[\exp \frac{m^*(\vartheta) | I_n - \tau_n(\xi, \vartheta, \epsilon^p) |}{k\vartheta} - 1 \right] + \frac{g^*(\xi, \vartheta)}{T_m \kappa_0} [I_g - \tau_{eq}(\xi, \vartheta, \epsilon^p)].$$

To have consistent theory of elasto-viscoplasticity we can replace the exponential function in the nucleation term and the linear function in the growth term by the empirical overstress Φ , then the evolution equation for the porosity ξ takes the form as follows (cf. PERZYNA [43])

$$(3.29) \quad \dot{\xi} = \frac{1}{T_m} h^*(\xi, \vartheta) \left\langle \Phi \left[\frac{I_n}{\tau_n(\xi, \vartheta, \epsilon^p)} - 1 \right] \right\rangle + \frac{1}{T_m} g^*(\xi, \vartheta) \left\langle \Phi \left[\frac{I_g}{\tau_{eq}(\xi, \vartheta, \epsilon^p)} - 1 \right] \right\rangle.$$

This determines the evolution function Ξ .

3.4. Thermodynamic restrictions and rate type constitutive equations

Suppose the axiom of the entropy production holds. Then the constitutive assumption (3.15) and the evolution equations (3.20) lead to the results as follows

$$(3.30) \quad \begin{aligned} \boldsymbol{\tau} &= \rho_{\text{Ref}} \frac{\partial \widehat{\psi}}{\partial \mathbf{e}}, & \eta &= -\frac{\partial \widehat{\psi}}{\partial \vartheta}, \\ -\frac{\partial \widehat{\psi}}{\partial \boldsymbol{\mu}} \cdot \mathbf{L}_{\mathbf{v}} \boldsymbol{\mu} - \frac{1}{\rho \vartheta} \mathbf{q} \cdot \text{grad } \vartheta &\geq 0. \end{aligned}$$

The rate of internal dissipation is determined by

$$(3.31) \quad \vartheta \widehat{i} = -\frac{\partial \widehat{\psi}}{\partial \boldsymbol{\mu}} \cdot \mathbf{L}_{\mathbf{v}} \boldsymbol{\mu} = -\left(\frac{\partial \widehat{\psi}}{\partial \epsilon^p} \sqrt{\frac{2}{3}} \right) \Lambda - \frac{\partial \widehat{\psi}}{\partial \xi} \Xi.$$

Operating on the stress relation (3.30)₁ with the Lie derivative and keeping the internal state vector constant, we obtain (cf. DUSZEK–PERZYNA and PERZYNA [15])

$$(3.32) \quad \mathbf{L}_{\mathbf{v}} \boldsymbol{\tau} = \mathcal{L}^e : \mathbf{d} - \mathcal{L}^{th} \dot{\vartheta} - [(\mathcal{L}^e + \mathbf{g} \boldsymbol{\tau} + \boldsymbol{\tau} \mathbf{g}) : \mathbf{P}] \frac{1}{T_m} \left\langle \Phi \left(\frac{f}{\kappa} - 1 \right) \right\rangle,$$

where

$$(3.33) \quad \mathcal{L}^e = \rho_{\text{Ref}} \frac{\partial^2 \widehat{\psi}}{\partial \mathbf{e}^2}, \quad \mathcal{L}^{th} = -\rho_{\text{Ref}} \frac{\partial^2 \widehat{\psi}}{\partial \mathbf{e} \partial \vartheta}.$$

Substituting $\widehat{\psi}$ into the energy balance equation and taking into account the results (3.30)₃ and (3.31) gives

$$(3.34) \quad \rho \vartheta \dot{\eta} = -\text{div} \mathbf{q} + \rho \widehat{i}.$$

Operating on the entropy relation (3.30)₂ with the Lie derivative and substituting the result into (3.34) we obtain

$$(3.35) \quad \rho c_p \dot{\vartheta} = -\text{div} \mathbf{q} + \vartheta \frac{\rho}{\rho_{\text{Ref}}} \frac{\partial \boldsymbol{\tau}}{\partial \vartheta} : \mathbf{d} + \rho \chi^* \boldsymbol{\tau} : \mathbf{d}^p + \rho \chi^{**} \dot{\xi},$$

where the specific heat

$$(3.36) \quad c_p = -\vartheta \frac{\partial^2 \widehat{\psi}}{\partial \vartheta^2}$$

and the irreversibility coefficients χ^* and χ^{**} are determined by

$$(3.37) \quad \begin{aligned} \chi^* &= -\left(\frac{\partial \widehat{\psi}}{\partial \epsilon^p} - \vartheta \frac{\partial^2 \widehat{\psi}}{\partial \vartheta \partial \epsilon^p} \right) \sqrt{\frac{2}{3}} \frac{1}{\boldsymbol{\tau} : \mathbf{P}}, \\ \chi^{**} &= -\left(\frac{\partial \widehat{\psi}}{\partial \xi} - \vartheta \frac{\partial^2 \widehat{\psi}}{\partial \vartheta \partial \xi} \right). \end{aligned}$$

So, a set of the constitutive equations of the rate type has the form as follows

$$\begin{aligned}
 \mathbf{L}_{\mathbf{v}}\boldsymbol{\tau} &= \mathcal{L}^e : \mathbf{d} - \mathcal{L}^{th}\dot{\vartheta} - [(\mathcal{L}^e + \mathbf{g}\boldsymbol{\tau} + \boldsymbol{\tau}\mathbf{g}) : \mathbf{P}] \frac{1}{T_m} \left\langle \Phi \left(\frac{f}{\kappa} - 1 \right) \right\rangle, \\
 \rho c_p \dot{\vartheta} &= -\operatorname{div} \mathbf{q} + \vartheta \frac{\rho}{\rho_{\text{Ref}}} \frac{\partial \boldsymbol{\tau}}{\partial \vartheta} : \mathbf{d} + \rho \chi^* \frac{1}{T_m} \left\langle \Phi \left(\frac{f}{\kappa} - 1 \right) \right\rangle \boldsymbol{\tau} : \mathbf{P} + \rho \chi^{**} \dot{\xi}, \\
 \dot{\xi} &= \frac{1}{T_m} h^*(\xi, \vartheta) \left\langle \Phi \left[\frac{I_n}{\tau_n(\xi, \vartheta, \epsilon^p)} - 1 \right] \right\rangle \\
 &\quad + \frac{1}{T_m} g^*(\xi, \vartheta) \left\langle \Phi \left[\frac{I_g}{\tau_{eq}(\xi, \vartheta, \epsilon^p)} - 1 \right] \right\rangle.
 \end{aligned}
 \tag{3.38}$$

All the material functions and the material constants should be identified based on available experimental data.

3.5. Fracture criterion based on the evolution of micro-damage

We base the fracture criterion on the evolution of the porosity internal state variable ξ . The volume fraction porosity ξ takes account for microdamage effects.

Let us assume that for $\xi = \xi^F$ catastrophe takes place (cf. PERZYNA [37]), that is

$$\kappa = \widehat{\kappa}(\epsilon^p, \vartheta, \xi)|_{\xi=\xi^F} = 0.
 \tag{3.39}$$

It means that for $\xi = \xi^F$ the material loses its carrying capacity. The condition (3.39) describes the main feature observed experimentally that the load tends to zero at the fracture point.

It is noteworthy that the isotropic hardening–softening material function $\widehat{\kappa}$ proposed in Eq. (3.22) should satisfy the fracture criterion (3.39).

3.6. Length-scale sensitivity of the constitutive model

The constitutive equations for a thermo-elastic-viscoplastic model introduce implicitly a length-scale parameter into the dynamic initial-boundary value problem, i.e.

$$l = \alpha c T_m,
 \tag{3.40}$$

where T_m is the relaxation time for mechanical disturbances, and is directly related to the viscosity of the material, c denotes the velocity of the propagation of the elastic waves in the problem under consideration, and the proportionality factor α depends on the particular initial-boundary value problem and may also be conditioned on the microscopic properties of the material.

The relaxation time T_m can be viewed either as a microstructural parameter to be determined from experimental observations or as a mathematical regularization parameter.

4. DISCUSSION OF THE EVOLUTION PROBLEM

4.1. Initial-boundary value problem (evolution problem)

Find $\boldsymbol{\varphi}$ as function of t and \mathbf{x} satisfying

$$(4.1) \quad \begin{cases} \text{(i)} & \dot{\boldsymbol{\varphi}} = \mathcal{A}(t, \boldsymbol{\varphi})\boldsymbol{\varphi} + \mathbf{f}(t, \boldsymbol{\varphi}); \\ \text{(ii)} & \boldsymbol{\varphi}(0) = \boldsymbol{\varphi}^0(\mathbf{x}); \\ \text{(iii)} & \text{The boundary conditions;} \end{cases}$$

where the unknown $\boldsymbol{\varphi}$ takes values in a Banach space, $\mathcal{A}(t, \boldsymbol{\varphi})$ is a spatial linear differential operator (in general unbounded) depending on t and $\boldsymbol{\varphi}$, \mathbf{f} is a nonlinear function, and the dot denotes the material derivative.

The evolution problem (4.1) describes an adiabatic inelastic flow process provided

$$(4.2) \quad \boldsymbol{\varphi} = \begin{bmatrix} \mathbf{v} \\ \rho \\ \boldsymbol{\tau} \\ \xi \\ \vartheta \end{bmatrix},$$

$$\mathbf{f} = \begin{bmatrix} 0 \\ 0 \\ -\frac{\langle \Phi \left(\frac{f}{\kappa} - 1 \right) \rangle}{T_m} \left[\left(\mathcal{L}^e + \frac{\chi^* \boldsymbol{\tau}}{\rho_{\text{Ref}}} \mathcal{L}^{th} + \mathbf{g}\boldsymbol{\tau} + \boldsymbol{\tau}\mathbf{g} \right) : \mathbf{P} \right] - \frac{\chi^{**} \Xi}{\rho_{\text{Ref}}} \mathcal{L}^{th} \\ \Xi \\ \frac{1}{T_m} \langle \Phi \left(\frac{f}{\kappa} - 1 \right) \rangle \frac{\chi^*}{\rho_{\text{Ref}}} \mathcal{L}^{th} \boldsymbol{\tau} : \mathbf{P} + \frac{\chi^{**}}{\rho_{\text{Ref}}} \Xi \end{bmatrix},$$

$$\mathcal{A} = \begin{bmatrix} 0 & 0 & \frac{\boldsymbol{\tau}}{\rho_{\text{Ref}} \rho} \text{grad} & \frac{1}{\rho_{\text{Ref}}} \text{div} & 0 \\ 0 & -\rho \text{div} & 0 & 0 & 0 \\ 0 & \mathbb{E} : \text{sym} \frac{\partial}{\partial \mathbf{x}} + 2 \text{sym} \left(\boldsymbol{\tau} : \frac{\partial}{\partial \mathbf{x}} \right) & 0 & 0 & 0 \\ 0 & 0 & 0 & 0 & 0 \\ 0 & \frac{\vartheta}{c_p \rho_{\text{Ref}}} \frac{\partial \boldsymbol{\tau}}{\partial \vartheta} : \text{sym} \frac{\partial}{\partial \mathbf{x}} & 0 & 0 & 0 \end{bmatrix}.$$

where

$$(4.3) \quad \mathbb{E} = \mathcal{L}^e - \frac{\vartheta}{c_p \rho_{\text{Ref}}} \mathcal{L}^{th} \frac{\partial \boldsymbol{\tau}}{\partial \vartheta}$$

denotes the thermo-elastodynamic matrix for adiabatic process.

It is noteworthy that the spatial operator \mathcal{A} has the same form as in thermo-elastodynamics while all dissipative effects generated by viscoplastic flow phenomena and by microdamage mechanisms influence the adiabatic impact loading process through the nonlinear function \mathbf{f} .

A strict solution of (4.1) with $\mathbf{f}(t, \boldsymbol{\varphi}) \equiv 0$ (i.e. the homogeneous evolution problem) is defined as a function $\boldsymbol{\varphi}(t) \in \mathbb{E}$ (a Banach space) such that⁵⁾

$$(4.4) \quad \begin{aligned} & \boldsymbol{\varphi}(t) \in \mathcal{D}(\mathcal{A}), & \text{for all } t \in [0, t_f], \\ & \lim_{\Delta t \rightarrow 0} \left\| \frac{\boldsymbol{\varphi}(t + \Delta t) - \boldsymbol{\varphi}(t)}{\Delta t} - \mathcal{A}\boldsymbol{\varphi}(t) \right\|_{\mathbb{E}} = 0 & \text{for all } t \in [0, t_f]. \end{aligned}$$

The boundary conditions are taken care of by restricting the domain $\mathcal{D}(\mathcal{A})$ to elements of \mathbb{E} that satisfy those conditions; they are assumed to be linear and homogeneous, so that the set \mathbf{S} of all $\boldsymbol{\varphi}$ that satisfy them is a linear manifold; $\mathcal{D}(\mathcal{A})$ is assumed to be contained in \mathbf{S} .

The choice of the Banach space \mathbb{E} , as well as the domain of \mathcal{A} , is an essential part of the formulation of the evolution problem.

4.2. Well-posedness of the evolution problem

The homogeneous evolution problem (i.e. for $\mathbf{f} \equiv 0$) is called well posed (in the sense of Hadamard) if it has the following properties:

- (i) The strict solutions are uniquely determined by their initial elements;
- (ii) The set Y of all initial elements of strict solutions is dense in the Banach space \mathbb{E} ;
- (iii) For any finite interval $[0, t_0]$, $t_0 \in [0, t_f]$ there is a constant $K = K(t_0)$ such that every strict solution satisfies the inequality

$$(4.5) \quad \|\boldsymbol{\varphi}(t)\| \leq K \|\boldsymbol{\varphi}^0\| \quad \text{for } 0 \leq t \leq t_0.$$

The inhomogeneous evolution problem (4.1) will be called well posed if it has a unique solution for all reasonable choices of $\boldsymbol{\varphi}^0$ and $\mathbf{f}(t, \boldsymbol{\varphi})$ and if the solution depends continuously, in some sense, on those choices.

⁵⁾We shall follow here some fundamental results which have been discussed in RICHTMYER and MORTON [47], STRANG and FIX [52], RICHTMYER [46] and DAUTRAY and LIONS [8].

It is evident that any solution is unique, because of the uniqueness of the solutions of the homogeneous evolution problem. Namely, the difference of two solutions, for given φ^0 and given $\mathbf{f}(\cdot)$, is a solution of the homogeneous problem with zero as initial element, hence must be zero for all t .

It is possible to show (cf. RICHTMYER [46]) that strict solutions exists for sets of φ^0 and $\mathbf{f}(\cdot)$ that are dense in E and E_1 (a new Banach space), respectively.

Let $\{\mathbb{F}_t^*; t \geq 0\}$ be a semi-group generated by the operator $\mathcal{A} + \mathbf{f}(\cdot)$ (as it has been defined in Section 4.1) and $\{\mathbb{F}_t; t \geq 0\}$ be a semi-group generated by the operator \mathcal{A} .

Then we can write the generalized solution of the nonhomogenous evolution problem (4.1) in alternative forms

$$\begin{aligned}
 \varphi(t, \mathbf{x}) &= \mathbb{F}^*(t)\varphi^0(\mathbf{x}) \\
 (4.6) \qquad &= \mathbb{F}(t)\varphi^0(\mathbf{x}) + \int_0^t \mathbb{F}(t-s)\mathbf{f}(s, \varphi(s))ds.
 \end{aligned}$$

The generalized solution of the nonhomogenous evolution problem (4.1) in the form (4.6)₂ is the integral equation.

The successive approximations for (4.6)₂ are defined to be the functions $\varphi_0, \varphi_1, \dots$, given by the formulas

$$\begin{aligned}
 \varphi_0(t) &= \varphi^0, \\
 &\dots\dots\dots \\
 (4.7) \qquad \varphi_{k+1}(t) &= \mathbb{F}(t)\varphi^0 + \int_0^t \mathbb{F}(t-s)\mathbf{f}(s, \varphi_k(s))ds, \\
 &k = 0, 1, 2, \dots; \quad t \in [0, t_f].
 \end{aligned}$$

It is possible to show that these functions actually exist on $t \in [0, t_f]$ if the continuous function \mathbf{f} is Lipschitz continuous with respect to the second argument uniformly with respect to $t \in [0, t_f]$, cf. PERZYNA [40]. Then (4.6)₂ has unique solution (cf. also IONESCU and SOFONEA [25]).

4.3. *Discretization in space and time*

We must approximate (4.1) twice. First, when E is infinite dimensional, we must replace \mathcal{A} by an operator \mathcal{A}_h which operates in a finite dimensional space $V_h \subset E$, where, in general, $h > 0$ represents a discretisation step in space, such that $\dim(V_h) \rightarrow \infty$ as $h \rightarrow 0$. Second, we must discretise in time, that is to say choose a sequence of moments t_n (for example $t_n = n\Delta t$, where Δt is time step) at which we shall calculate the approximate solution.

Let us introduce the following semi-discretised (discrete in space) problem.

$$(4.8) \quad \left\{ \begin{array}{l} \text{Find } \boldsymbol{\varphi}_h \in \mathcal{C}^0([0, t_0]; V_h) \text{ (} \mathcal{C}^0 \text{ denotes the space of functions} \\ \text{continuous on } ([0, t_0], V_h) \text{) satisfying} \\ \frac{d\boldsymbol{\varphi}_h(t)}{dt} = \mathcal{A}_h \boldsymbol{\varphi}_h(t) + \mathbf{f}_h(t), \\ \boldsymbol{\varphi}_h(0) = \boldsymbol{\varphi}_{0,h}. \end{array} \right.$$

The operator \mathcal{A}_h for the finite element method can be obtained by a variational formulation approach. The discrete equations are obtained by the Galerkin method at particular points in the domain.

Finally, we shall define a method allowing us to calculate $\boldsymbol{\varphi}_h^n \in V_h$, an approximation to $\boldsymbol{\varphi}_h(t_n)$ starting from $\boldsymbol{\varphi}_h^{n-1}$ (we limit ourselves to a two-level scheme). Then we can write

$$(4.9) \quad \boldsymbol{\varphi}_h^{n+1} = C_h(\Delta t) \boldsymbol{\varphi}_h^n + \Delta t \mathbf{f}_h^n, \quad \boldsymbol{\varphi}_h^0 = \boldsymbol{\varphi}_{0,h},$$

where we introduce the operator $C_h(\Delta t) \in \mathcal{L}(V_h)$ (\mathcal{L} is the set of continuous linear mapping of V_h with values in V_h) and where \mathbf{f}_h^n approximates $\mathbf{f}_h(t_n)$.

We shall always assume that the evolution problem (4.1) is well posed and there exists a projection R_h of E into V_h such that

$$(4.10) \quad \lim_{h \rightarrow 0} |R_h \boldsymbol{\varphi} - \boldsymbol{\varphi}|_E = 0, \quad \forall \boldsymbol{\varphi} \in E.$$

4.4. Convergence, consistency and stability

The first fundamental question is that of the convergence, when h and Δt tend to zero, of the sequence $\{\boldsymbol{\varphi}_h^n\}$, the solution (4.9), towards the function $\boldsymbol{\varphi}(t)$, the solution of (4.1). Let us restrict our consideration, for the moment, to the case where $\mathbf{f}(t) \equiv 0$.

DEFINITION 1: *The scheme defined by (4.9) will be called convergent if the condition*

$$(4.11) \quad \boldsymbol{\varphi}_{0,h} \rightarrow \boldsymbol{\varphi}^0 \quad \text{as } h \rightarrow 0$$

implies that

$$(4.12) \quad \boldsymbol{\varphi}_h^n \rightarrow \boldsymbol{\varphi}(t) \quad \text{as } \Delta t \rightarrow 0, \quad n \rightarrow \infty \quad \text{with } n\Delta t \rightarrow t$$

for all $t \in]0, t_0[$, $t_0 \in [0, t_f]$, where $\boldsymbol{\varphi}_h^n$ is defined by (4.9) and $\boldsymbol{\varphi}(t)$ is the solution of (4.1). All this holds for arbitrary $\boldsymbol{\varphi}^0$.

The study of the convergence of an approximation scheme involves two fundamental properties of the scheme, consistency and stability.

DEFINITION 2: *The scheme defined by (4.9) is called stable, if there exists a constant $K \geq 1$ independent of h and Δt such that*

$$(4.13) \quad \|(C_h(\Delta t))^n R_h\|_{\mathcal{L}(E)} \leq K \quad \forall n, \Delta t \text{ satisfying } n\Delta t \leq t_0.$$

In the Definition 1 and 2 there occur two parameters h and Δt . It may be that the scheme is not stable (or not convergent) unless Δt and h satisfy supplementary hypotheses of the type $\Delta t/h^\alpha \leq \text{constant}$, $\alpha < 0$, in which case we call the scheme **conditionally stable**. If the scheme is stable for arbitrary h and Δt we say that it is **unconditionally stable**.

These schemes reflect so called explicit and implicit types of the integration procedure in a particular umerical implementation.

DEFINITION 3: *The scheme defined by (4.9) will be called consistent with equation (4.1) if there exists a subspace $Y \subset E$ dense in E , such that for every $\boldsymbol{\varphi}(t)$ which is a solution of (4.1) with $\boldsymbol{\varphi}^0 \subset Y$ (and $\mathbf{f} \equiv 0$) we have*

$$(4.14) \quad \lim_{h \rightarrow 0, \Delta t \rightarrow 0} \left| \frac{C_h(\Delta t) R_h \boldsymbol{\varphi}(t) - \boldsymbol{\varphi}(t)}{\Delta t} - \mathcal{A} \boldsymbol{\varphi}(t) \right|_E = 0.$$

We see that the two essential preoccupations in the study of approximation schemes for the solution of evolution equations are on the one hand the determination of the consistency of the scheme, more precisely the order of precision and on the other hand its stability.

Determining the order of precision is, in general, easy, we shall therefore study the stability of the scheme in more detail.

4.5. The Lax-Richtmyer equivalence theorem

We can now state the Lax-Richtmyer equivalence theorem (cf. RICHTMYER and MORTON [47], STRANG and FIX [52], DAUTRAY and LIONS [8] and GUSTAFSSON, KREISS and OLIGER [23]).

THEOREM 1: *Suppose that the evolution problem (4.1) is well-posed for $t \in [0, t_0]$ and that it is approximated by the scheme (4.9), which we assume consistent. Then the scheme is convergent if and only if it is stable.*

The proof of the Lax-Richtmyer equivalence theorem for the case when the partial differential operator \mathcal{A} in (4.2) is independent of $\boldsymbol{\varphi}$ can be found in DAUTRAY and LIONS [8].

REMARK. Let us consider the evolution problem (4.1) with

$$(4.15) \quad \mathbf{f}(t, \boldsymbol{\varphi}) \neq 0$$

and $\boldsymbol{\varphi}^0 = 0$, and also the corresponding approximation (4.9). We have

$$(4.16) \quad \boldsymbol{\varphi}_h^{n+1} = \Delta t \sum_{j=1}^n [C_h(\Delta t)]^{n-j} \mathbf{f}_h^j.$$

If \mathcal{A} is the infinitesimal generator of a semigroup $\{\mathbb{F}(t)\}$ we can write

$$(4.17) \quad \boldsymbol{\varphi}(t) = \int_0^t \mathbb{F}(t-s) \mathbf{f}(s) ds.$$

Under suitable hypotheses on the convergence of \mathbf{f}_h^j to $\mathbf{f}(j\Delta t)$ we can show that expression (4.16) converges to (4.17) if the scheme is stable and consistent.

4.6. Dispersive analysis

The most important feature is that the propagation of deformation waves in an elastic-viscoplastic medium has dispersive nature.

The dispersion of a waveform is caused by certain physical and/or geometrical characteristics of the medium in which the wave is generated. Consequently, instead of dispersive waves, it is perhaps more precise to speak of a **dispersive medium** or, where geometrical features alone cause the dispersion, a **dispersive geometry**, cf. THAU [53].

To make our analysis easier let us consider the linear case of the evolution equation with the interpretation of the functions $\boldsymbol{\varphi}$ and \mathbf{f} as well as the spatial differential operator \mathcal{A} given by (4.1) and (4.2) i.e.

$$(4.18) \quad \dot{\boldsymbol{\varphi}} = \mathcal{A}_0(t, \mathbf{x}) \boldsymbol{\varphi} + f_0(t, \mathbf{x}) \boldsymbol{\varphi}.$$

The theory of dispersive wave propagation can be introduced by a particular wave solution of (4.18), namely, by the simple harmonic wavetrains (cf. WHITHAM [55, 56] and THAU [53])

$$(4.19) \quad \boldsymbol{\varphi} = A \exp[i(\mathbf{k} \cdot \mathbf{x} - \omega t)],$$

where \mathbf{k} is the wave number, ω is the frequency, and A denotes the amplitude.

Since a set of the equations (4.18) is linear, A factor out and can be arbitrary. To satisfy a set of the equations (4.18), \mathbf{k} and ω have to be related by an equation

$$(4.20) \quad G(\omega, \mathbf{k}, \mathbf{x}, t) = 0,$$

which is called the dispersion relation.

Let us assume that the dispersion relation may be solved in the form of real roots

$$(4.21) \quad \omega = W(\mathbf{k}, \mathbf{x}, t).$$

There will be a number of such solutions, in general, with different functions $W(\mathbf{k}, \mathbf{x}, t)$. We refer to these as different modes.

The phase velocity \mathbf{c} is given as a function of wavenumber

$$(4.22) \quad \mathbf{c}(\mathbf{k}, \mathbf{x}, t) = \frac{\omega}{k} \hat{\mathbf{k}} = k^{-1} W(\mathbf{k}, \mathbf{x}, t) \hat{\mathbf{k}},$$

where $\hat{\mathbf{k}}$ is the unit vector in the \mathbf{k} direction. For any particular mode $\omega = W(\mathbf{k}, \mathbf{x}, t)$, the phase velocity \mathbf{c} is a function of \mathbf{k} .

Another velocity associated with the harmonic wavetrains (4.19) in dispersive media is the group velocity \mathbf{C} defines as

$$(4.23) \quad \mathbf{C}(\mathbf{k}, \mathbf{x}, t) = \frac{\partial W(\mathbf{k}, \mathbf{x}, t)}{\partial \mathbf{k}},$$

which also depends on the wavenumber \mathbf{k} .

The derivative of \mathbf{C} with respect to \mathbf{k} is the symmetric dispersive tensor

$$(4.24) \quad W_{\mathbf{k}\mathbf{k}} = \frac{\partial^2 W}{\partial \mathbf{k}^2}.$$

To have dispersive wave we have to introduce two assertions:

$$(4.25) \quad \begin{aligned} (i) \quad & W(\mathbf{k}, \mathbf{x}, t) \text{ is real;} \\ (ii) \quad & \det \left| \frac{\partial^2 W}{\partial k_i \partial k_j} \right| \neq 0. \end{aligned}$$

The group velocity \mathbf{C} is having a great effect and the condition (4.25)₂ ensures that it is not a constant.

The quantity

$$(4.26) \quad \Theta = \mathbf{k} \cdot \mathbf{x} - \omega t$$

in the solution (4.19) is the phase. The group velocity is actually the most important velocity associated with dispersive waves, as it not only is the velocity of a given group of oscillations or “wavelets” in a wavetrain but also coincides with the velocity with which the energy in that group propagates. Moreover, in a dispersive medium any initial disturbance is eventually broken up into a system of such groups, cf. THAU [53].

Since the medium under consideration has also dissipation property (cf. Eq. (4.1) in which the last term on the right hand side is responsible for dissipation effect) hence mathematically, losses due to dissipation are manifested by the dispersion relation yielding complex or pure imaginary values of W corresponding to real values of \mathbf{k} . The amplitude of a harmonic wavetrain then decays exponentially with time.

If the dissipation becomes appreciable, as is in the elastic-viscoplastic medium, then the general theory of waves in dispersive media would require modification.

The previous consideration does not apply to general nonlinear case (cf. Eq. (4.1)). To obtain some results we can use the variational method, the perturbation theory or the numerical method, cf. SLUYS [51].

Dispersion is a relation between the frequency and wave number, cf. WHITHAM [55]. The ratio of the frequency and wave number is the phase speed whereas the derivative of the frequency with respect to the wave number is the group speed. For nondispersive problem, both speeds are equal and on the other hand for dispersive one the group velocity depends on the frequency and in general is different from the phase speed. As a matter of fact, the dispersion of a waveform is caused by both material (physical law) and geometrical (boundaries) characteristics of the medium (specimen) in which the wave is generated.

4.7. Application of finite difference method

Let us consider the evolution problem in the form of (4.1). Let us introduce in the Euclidean space E^3 a regular difference net of nodes (i, j, k) with convective coordinates $\chi_i^1 = i\Delta\chi^1$, $\chi_j^2 = j\Delta\chi^2$ and $\chi_k^3 = k\Delta\chi^3$, $i, j, k \in N$, where N is a set of natural numbers, cf. DORNOWSKI [10] and DORNOWSKI and PERZYNA [11]. Of course, some of the nodes belong to the edge of the body and are used to approximate the boundary conditions. Time is approximated by a discrete sequence of moments $t_n = n\Delta t$, where Δt is time step, $n \in N$.

For all functions $\boldsymbol{\varphi} = \widehat{\boldsymbol{\varphi}}(\mathbf{x}, t)$ of the analysed problem we postulate the following approximation in the domain $\Delta E = \Delta\chi^1 \times \Delta\chi^2 \times \Delta\chi^3$ of a convective difference mesh (cf. Fig. 9):

$$(4.27) \quad \boldsymbol{\varphi}(\mathbf{x}, t) \cong \boldsymbol{\varphi}_h(\mathbf{x}, t) = \mathbf{a}_1(t) + \mathbf{a}_2(t)\chi^1 + \mathbf{a}_3(t)\chi^2 + \mathbf{a}_4(t)\chi^3 \\ + \mathbf{a}_5(t)\chi^1\chi^2 + \mathbf{a}_6(t)\chi^1\chi^3 + \mathbf{a}_7(t)\chi^2\chi^3 + \mathbf{a}_8(t)\chi^1\chi^2\chi^3,$$

$$\mathbf{x} \in \Delta\mathcal{S}.$$

The functions $\mathbf{a}_1(t), \dots, \mathbf{a}_8(t)$ depend only on time, are determined by the value of the function $\boldsymbol{\varphi}_w(t) = [\boldsymbol{\varphi}_1(t), \dots, \boldsymbol{\varphi}_8(t)]^T$ in the node points of difference

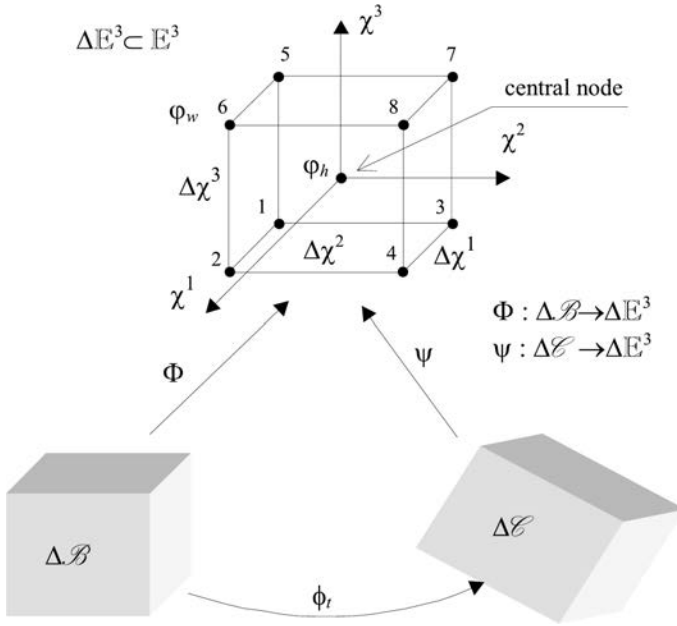


FIG. 9. Convective finite difference mesh of nodes.

mesh, (cf. Fig. 9). Hence the approximation functions (4.27) can be written in the form

$$(4.28) \quad \boldsymbol{\varphi}_h(\mathbf{x}, t) = \mathbf{N}(\mathbf{x})\boldsymbol{\varphi}_w(t), \quad \mathbf{x} \in \Delta\mathcal{S},$$

where

$$(4.29) \quad \begin{aligned} N_1(\mathbf{x}) &= q(-\Delta\chi^1 + 2\chi^1)(-\Delta\chi^2 + 2\chi^2)(\Delta\chi^3 - 2\chi^3), \\ N_2(\mathbf{x}) &= q(\Delta\chi^1 + 2\chi^1)(-\Delta\chi^2 + 2\chi^2)(-\Delta\chi^3 + 2\chi^3), \\ N_3(\mathbf{x}) &= q(-\Delta\chi^1 + 2\chi^1)(\Delta\chi^2 + 2\chi^2)(-\Delta\chi^3 + 2\chi^3), \\ N_4(\mathbf{x}) &= q(\Delta\chi^1 + 2\chi^1)(\Delta\chi^2 + 2\chi^2)(\Delta\chi^3 - 2\chi^3), \\ N_5(\mathbf{x}) &= q(-\Delta\chi^1 + 2\chi^1)(-\Delta\chi^2 + 2\chi^2)(\Delta\chi^3 + 2\chi^3), \\ N_6(\mathbf{x}) &= q(\Delta\chi^1 + 2\chi^1)(\Delta\chi^2 - 2\chi^2)(\Delta\chi^3 + 2\chi^3), \\ N_7(\mathbf{x}) &= q(\Delta\chi^1 - 2\chi^1)(\Delta\chi^2 + 2\chi^2)(\Delta\chi^3 + 2\chi^3), \\ N_8(\mathbf{x}) &= q(\Delta\chi^1 + 2\chi^1)(\Delta\chi^2 + 2\chi^2)(\Delta\chi^3 + 2\chi^3), \\ q &= \frac{1}{8\Delta\chi^1\Delta\chi^2\Delta\chi^3} \end{aligned}$$

Equations (4.28) allow to determine values of the function $\boldsymbol{\varphi}_h(\mathbf{x}, t)$ in any point of the difference mesh, $\mathbf{x} \in \Delta\mathcal{S}$. For the central point $\mathbf{x} = \mathbf{x}_0$, $N_1 = \dots = N_8 = \frac{1}{8}$ and $\boldsymbol{\varphi}_h(t) = [\boldsymbol{\varphi}_1(t) + \dots + \boldsymbol{\varphi}_8(t)]\frac{1}{8}$.

By using (4.28) we can determine the matrix of the difference operators which approximate the first partial derivatives of the function $\boldsymbol{\varphi}(\mathbf{x}, t)$ for $\mathbf{x} \in \Delta\mathcal{S}$,

$$(4.30) \quad \frac{\partial}{\partial \mathbf{x}} \boldsymbol{\varphi}(\mathbf{x}, t) \cong \frac{\partial}{\partial \mathbf{x}} \boldsymbol{\varphi}_h(\mathbf{x}, t) = \frac{\partial}{\partial \mathbf{x}} \mathbf{N}(\mathbf{x}) \boldsymbol{\varphi}_w(t) = \mathbf{R}(\mathbf{x}) \boldsymbol{\varphi}_w(t).$$

The matrix of the difference operator $\mathbf{R}(\mathbf{x})$ for the central point takes the form

$$(4.31) \quad \mathbf{R}(\mathbf{x} = \mathbf{x}_0) = \left. \frac{\partial}{\partial \mathbf{x}} \mathbf{N}(\mathbf{x}) \right|_{\mathbf{x}=\mathbf{x}_0} = \begin{bmatrix} \frac{-1}{\Delta\chi^1} & \frac{1}{\Delta\chi^1} & \frac{-1}{\Delta\chi^1} & \frac{1}{\Delta\chi^1} & \frac{-1}{\Delta\chi^1} & \frac{1}{\Delta\chi^1} & \frac{-1}{\Delta\chi^1} & \frac{1}{\Delta\chi^1} \\ \frac{-1}{\Delta\chi^2} & \frac{-1}{\Delta\chi^2} & \frac{1}{\Delta\chi^2} & \frac{1}{\Delta\chi^2} & \frac{-1}{\Delta\chi^2} & \frac{-1}{\Delta\chi^2} & \frac{1}{\Delta\chi^2} & \frac{1}{\Delta\chi^2} \\ \frac{-1}{\Delta\chi^3} & \frac{-1}{\Delta\chi^3} & \frac{-1}{\Delta\chi^3} & \frac{-1}{\Delta\chi^3} & \frac{1}{\Delta\chi^3} & \frac{1}{\Delta\chi^3} & \frac{1}{\Delta\chi^3} & \frac{1}{\Delta\chi^3} \end{bmatrix}.$$

In similar way we can find the difference form of the spatial difference operator $\mathcal{A}(t, \boldsymbol{\varphi})$ of the considered evolution problem (4.1)

$$(4.32) \quad \mathcal{A}(t, \boldsymbol{\varphi}) \boldsymbol{\varphi} \cong \mathcal{A}(t, \boldsymbol{\varphi}_h) \mathbf{N}(\mathbf{x}) \boldsymbol{\varphi}_w(t) = \mathcal{A}_h(t, \boldsymbol{\varphi}_h) \boldsymbol{\varphi}_w(t),$$

hence

$$(4.33) \quad \mathcal{A}_h(t, \boldsymbol{\varphi}_h) = \mathcal{A}(t, \boldsymbol{\varphi}_h) \mathbf{N}(\mathbf{x}) \quad \text{for} \quad \mathbf{x} \in \Delta\mathcal{S}.$$

For the central node, $\mathbf{x} = \mathbf{x}_0$ the difference operator (4.33) depends only on time.

As a result of the proposed approximation of the evolution problem (4.1) with respect to the spatial variables we obtain a set of differential equations with respect to time and difference equations with respect to spatial variables

$$(4.34) \quad \frac{d\boldsymbol{\varphi}_h(t)}{dt} = \mathcal{A}_h \boldsymbol{\varphi}_w(t) + \mathbf{f}_h(t).$$

For the approximation of (4.34) with respect to time we use the evident scheme of the first order in the form

$$(4.35) \quad \frac{d\boldsymbol{\varphi}_h(t)}{dt} \cong \frac{\boldsymbol{\varphi}_h^{n+1} - \boldsymbol{\varphi}_h^n}{\Delta t} = \mathcal{A}_h \boldsymbol{\varphi}_w^n + \mathbf{f}_h^n.$$

The solution of (4.35) is reduced to the realization of the recurrence relation

$$(4.36) \quad \boldsymbol{\varphi}_h^{n+1} = \mathbf{C}_h(\Delta t)\boldsymbol{\varphi}_w^n + \Delta t\mathbf{f}_h^n.$$

The difference operator

$$(4.37) \quad \mathbf{C}_h(\Delta t) = \Delta t\mathcal{A}_h + \mathbf{N}$$

couple dependent variables and various points of difference mesh.

For the finite difference approximation it can be proved that the introduced scheme (4.36) is consistent with equation (4.1).

4.8. Stability criterion

In explicit finite difference scheme for a set of the partial differential equations (4.1)₁ of the hiperbolic type the condition of stability is assumed as the criterion of Courant–Friedrichs–Lewy, cf. COURANT *et al.* [6]

$$(4.38) \quad \Delta t_{n,n+1} \leq \min \left(\frac{\Delta L_{p,q,r}^n}{|c_{p,q,r}^n|} \right),$$

$$p = 1, 2, 3, \dots, P; \quad q = 1, 2, 3, \dots, Q; \quad r = 1, 2, 3, \dots, R,$$

where $\Delta t_{n,n+1}$ denotes time step, $c_{p,q,r}^n$ denotes the velocity of the propagation of the disturbances in the vicinity of the central node (p, q, r) , $\Delta L_{p,q,r}^n$ is the minimum distance between the mesh nodes which are in the vicinity of the node (cf. Fig. 9).

The Courant–Friedrichs–Lewy condition requires that the numerical domain of dependence of a finite-difference scheme include the domain of dependence of the associated partial differential equations, cf. DURRAN [16].

We can now use the Lax–Richtmyer equivalence theorem (cf. Theorem 1 in Subsec. 4.5).

5. IDENTIFICATION PROCEDURE

5.1. Assumption of the material functions for an adiabatic process

To do the proper identification procedure we first make assumption of the material functions (cf. DORNOWSKI and PERZYNA [11]).

The plastic potential function f is assumed in the form (cf. PERZYNA [37] and SHIMA and OYANE [48])

$$(5.1) \quad f = \left\{ J_2' + [n_1(\vartheta) + n_2(\vartheta)\xi] J_1^2 \right\}^{1/2}$$

where

$$(5.2) \quad \begin{aligned} n_1(\vartheta) &= 0, \\ n_2(\vartheta) &= n = \text{const.} \end{aligned}$$

The isotropic work-hardening-softening function κ is postulated as (cf. PERZYNA [38] and NEMES and EFTIS [32])

$$(5.3) \quad \begin{aligned} \kappa &= \widehat{\kappa}(\epsilon^p, \vartheta, \xi) \\ &= \{\kappa_s(\vartheta) - [\kappa_s(\vartheta) - \kappa_0(\vartheta)] \exp[-\delta(\vartheta)\epsilon^p]\} \left[1 - \left(\frac{\xi}{\xi_F} \right)^{\beta(\vartheta)} \right], \end{aligned}$$

where

$$(5.4) \quad \begin{aligned} \kappa_s(\vartheta) &= \kappa_s^*(1 - \bar{\nu}), & \kappa_0(\vartheta) &= \kappa_0^*(1 - \bar{\nu}), \\ \delta(\vartheta) &= \delta^*(1 - \bar{\nu}), & \beta(\vartheta) &= \beta^*(1 - \bar{\nu}), & \bar{\nu} &= \frac{\vartheta - \vartheta_0}{\vartheta_0}. \end{aligned}$$

The overstress function $\Phi\left(\frac{f}{\kappa} - 1\right)$ is assumed in the form

$$(5.5) \quad \Phi\left(\frac{f}{\kappa} - 1\right) = \left(\frac{f}{\kappa} - 1\right)^m.$$

The evolution equation for the porosity ξ is postulated as

$$(5.6) \quad \dot{\xi} = \dot{\xi}_{\text{grow}} = \frac{g^*(\xi, \vartheta)}{T_m \kappa_0(\vartheta)} [I_g - \tau_{eq}(\xi, \vartheta, \epsilon^p)]$$

where (cf. DORNOWSKI [9])

$$(5.7) \quad \begin{aligned} g^*(\xi, \vartheta) &= c_1(\vartheta) \frac{\xi}{1 - \xi}, \\ I_g &= b_1 J_1 + b_2 \sqrt{J_2}, \\ \tau_{eq}(\xi, \vartheta, \epsilon^p) &= c_2(\vartheta)(1 - \xi) \ln \frac{1}{\xi} \{2\kappa_s(\vartheta) - [\kappa_s(\vartheta) - \kappa_0(\vartheta)] F(\xi_0, \xi, \vartheta)\}, \\ c_1(\vartheta) &= \text{const}, & c_2(\vartheta) &= \text{const}, \end{aligned}$$

$$F(\xi_0, \xi, \vartheta) = \left(\frac{\xi_0}{1 - \xi_0} \frac{1 - \xi}{\xi} \right)^{\frac{2}{3}\delta} + \left(\frac{1 - \xi}{1 - \xi_0} \right)^{\frac{2}{3}\delta}.$$

As in the infinitesimal theory of elasticity we assume linear properties of the material, i.e.

$$(5.8) \quad \mathcal{L}^e = 2\mu\mathbf{I} + \lambda(\mathbf{g} \otimes \mathbf{g}),$$

where μ and λ denote the Lamé constants, and the thermal expansion matrix is postulated as

$$(5.9) \quad \mathcal{L}^{th} = (2\mu + 3\lambda)\theta\mathbf{g},$$

where θ is the thermal expansion constant ($\theta = 12 \cdot 10^{-6} \text{ K}^{-1}$).

5.2. Identification of the material constants

To determine the material constants assumed in Subsec. 5.1 we take advantage of the experimental observations presented by CHAKRABARTI and SPRETNAK [2]. They investigated the localized fracture mode for tensile steel sheet specimens simulating both plane stress and plane strain processes. The material used in their study was AISI 4340 steel. The principal variable in this flat specimen test was the width-to-thickness ratio. Variation in specimen geometry produces significant changes in stress state, directions of shear bands, and ductility. They found that fracture propagated consistently along the shear band localized region.

Let us now consider the adiabatic dynamic process for a thin steel plate under condition of plane stress state. In fact we idealize the initial-boundary value problem investigated by CHAKRABARTI and SPRETNAK [2] by assuming the velocity driven adiabatic process for a thin steel plate. Dimensions of the plate and the variation in time of the kinematic constraints are presented in Fig. 10. The problem has been solved by using the finite difference method. A thin sheet is modelled via $N \times M$ elements, cf. Fig. 10.

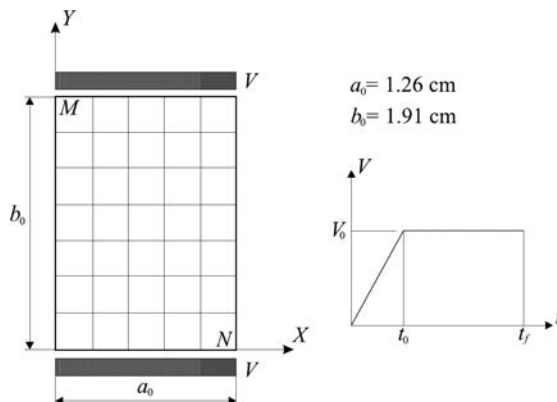


FIG. 10. Dimension of the plate and the variation in time of the kinematic constraints (after CHAKRABARTI and SPRETNAK [2]).

In numerical calculations it is assumed:

$$\begin{aligned} V_0 &= 1.5 \text{ m/s,} \\ t_0 &= 50 \text{ } \mu\text{s,} \\ t_f &= 800 \text{ } \mu\text{s.} \end{aligned}$$

The material of a plate is AISI 4340 steel.

Based on the best curve fitting of the experimental results obtained by CHAKRABARTI and SPRETNAK [2] for the stress-strain relation (cf. Fig. 11) the identification of the material constants has been done, cf. Table 1.

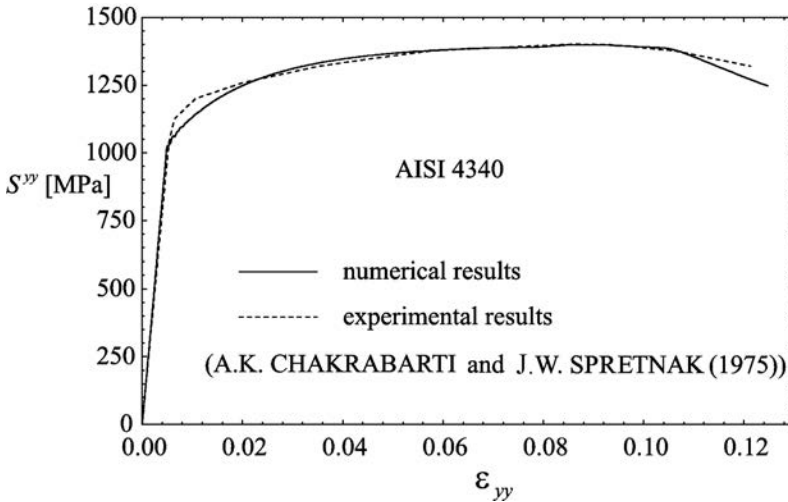


FIG. 11. Component S^{YY} of the second Piola–Kirchhoff stress tensor S as a function of the logarithmic strain ϵ_{YY} .

Table 1. An AISI 4340 steel (plate).

$\kappa_s^* = 1155 \text{ MPa}$	$\vartheta_0 = 293 \text{ K}$	$c_1 = 0.1$	$\xi_0 = 6 \cdot 10^{-4}$	$\nu = 0.3$
$\kappa_0^* = 808 \text{ MPa}$	$\iota = 0.1$	$c_2 = 0.067$	$\xi_F = 0.25$	$E = 208 \text{ GPa}$
$\delta^* = 14$	$T_m = 1 \text{ } \mu\text{s}$	$b_1 = 0.58$	$n = 0.25$	$\rho_{\text{Ref}} = 7850 \text{ kg/m}^3$
$\beta^* = 9$	$m = 1$	$b_2 = 1.73$	$\chi = 0.9$	$c_p = 455 \text{ J/kg K}$

5.3. Investigation of stability and convergence

Using the same initial-boundary value problem we can investigate the convergence of the numerical method based on the finite difference discretization. In this analysis we assume that the micro-damage evolution is investigated. For a thin steel plate five different meshes have been assumed. In Fig. 12 distributions of the equivalent plastic deformation along the middle cross-section

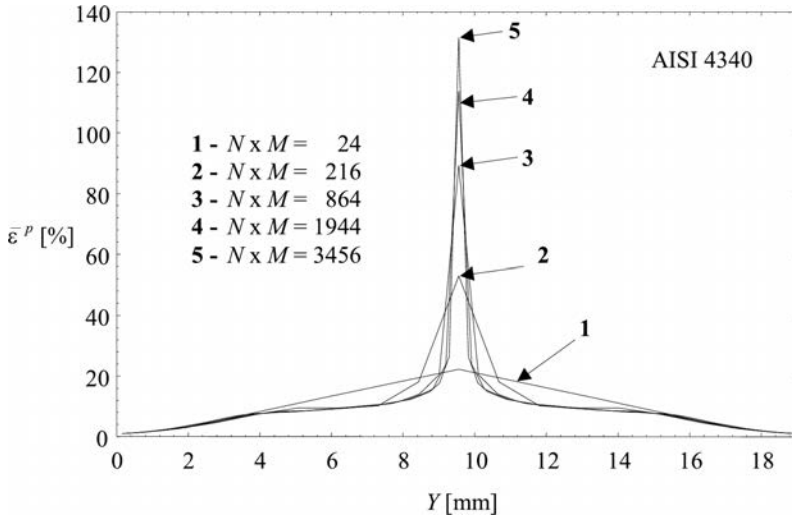


FIG. 12. Distributions of the equivalent plastic deformation along the middle cross-section ($X = a_0/2$) for various meshes.

($X = a_0/2$) for various meshes are presented. Similar results for temperature are showed in Fig. 13. All curves are plotted in the initial configuration of the specimen and for finite time of the process, $t_f = 800 \mu\text{s}$. The deformed meshes with various densities of nodes are presented in Fig. 14. Both analysed values shown in Fig. 12 and 13 have strong increase in the middle region of the plate. This suggests that in that region of the specimen the localization of plastic de-

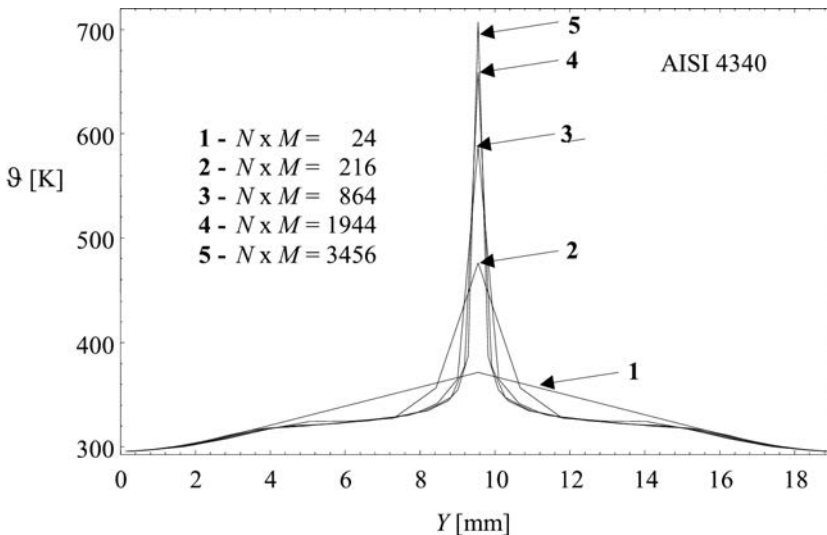


FIG. 13. Distributions of the temperature along the middle cross-section ($X = a_0/2$) for various meshes.

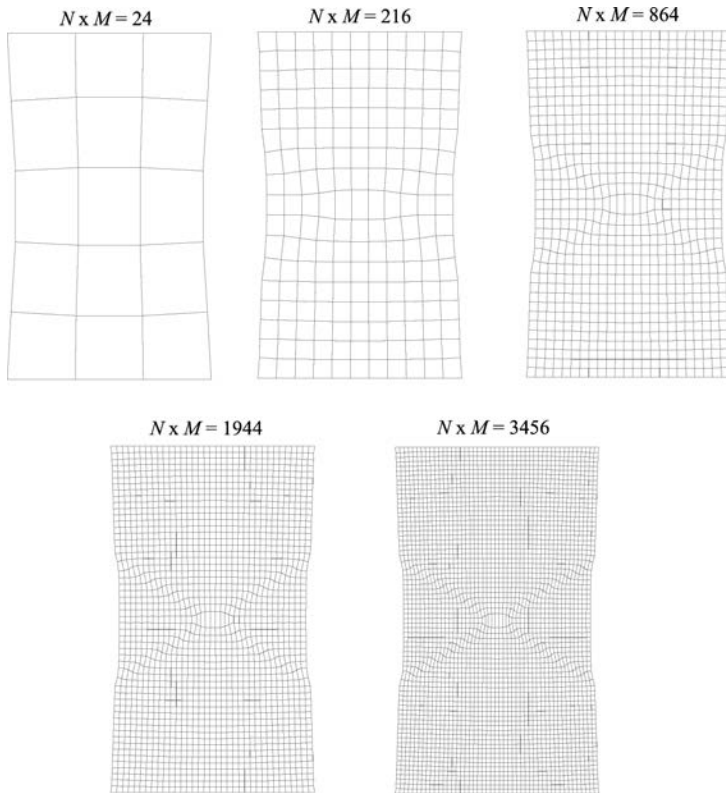


FIG. 14. Deformed meshes with various densities of nodes.

formation takes place. Based on the results for distributions of the equivalent plastic deformation plotted in Fig. 12 we can observe that the finite width of the localized region needs appropriate density for the finite difference mesh (in considered case higher than 864 nodes).

The numerical procedure for the explicit finite difference scheme (4.36) has been accomplished with various time step Δt . The value of the time step has been determined by using the stability criterion (4.38). In Fig. 15 the evolution of the time step Δt in the deformation process for the mesh $N \times M = 3456$ has been shown. For the considered deformation process the time step Δt is decreasing function of time.

The stability of the numerical procedure with constant time step can be keeping in entire interval $[0, t_f]$ provided we assume $\Delta t = 0.025 \mu\text{s}$. Then as a result for the considered deformation process we have 32 000 time steps. While the analogical process with various time step Δt is accomplished for 26 603 time steps. This decreases very much time of computation. Very intense change of time step Δt observed from $t = 0.6 \text{ ms}$ in Fig. 15 is caused by the formation of the shear band localization.

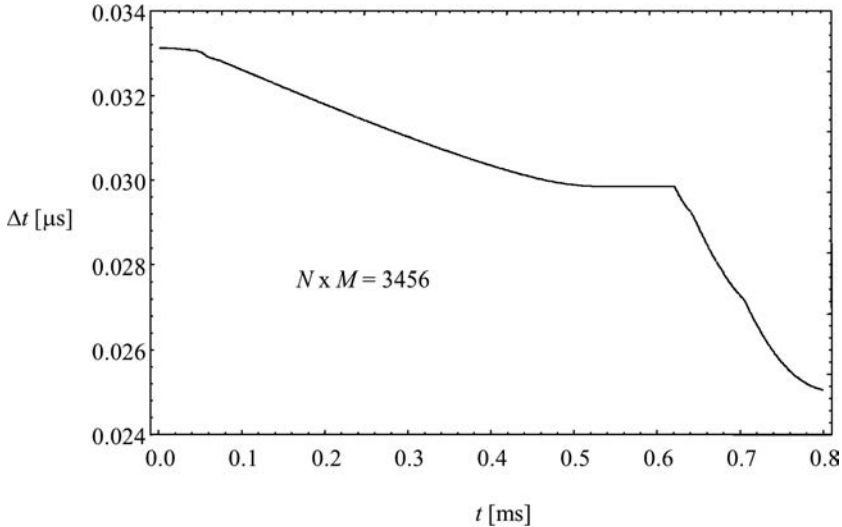


FIG. 15. Evolution of the time step Δt for a mesh with 3456 nodes.

The results obtained show that the satisfaction of the stability criterion (4.38) leads to the convergence of the numerical procedure. We can conclude that the assumed finite difference scheme (4.36) approximates the well posed initial-boundary value problem (4.1). These results can be treated as the numerical proof of the Lax–Richtmyer equivalence theorem formulated in Subsec. 4.8.

5.4. Investigation of localization and fracture phenomena

Let us consider again the adiabatic dynamic process for a thin steel plate under condition of plane stress state which idealized the experimental observations of the localized fracture mode for tensile steel sheet specimens performed by CHAKRABARTI and SPRETNAK [2], cf. Subsec. 5.2.

In Fig. 16 distributions of the equivalent plastic deformation in a thin plate for chosen instants of the deformation process are presented.

The development of macrocracks in a thin plate has been shown in Figs. 17 and 18 and the deformed configuration for final fracture of a plate is presented in Fig. 19.

The results presented permit to draw some conclusions concerning the adiabatic dynamic deformation process for a thin steel plate considered. We observe that two cross shear bands are developed in the center of the specimen. With continued loading process, one of the instability bands becomes more predominant and most of the plastic deformation is confirmed to this particular adiabatic shear band. Fracture occurs along the boundary of this active instability band. The symmetry breaking in the deformation process observed is only due

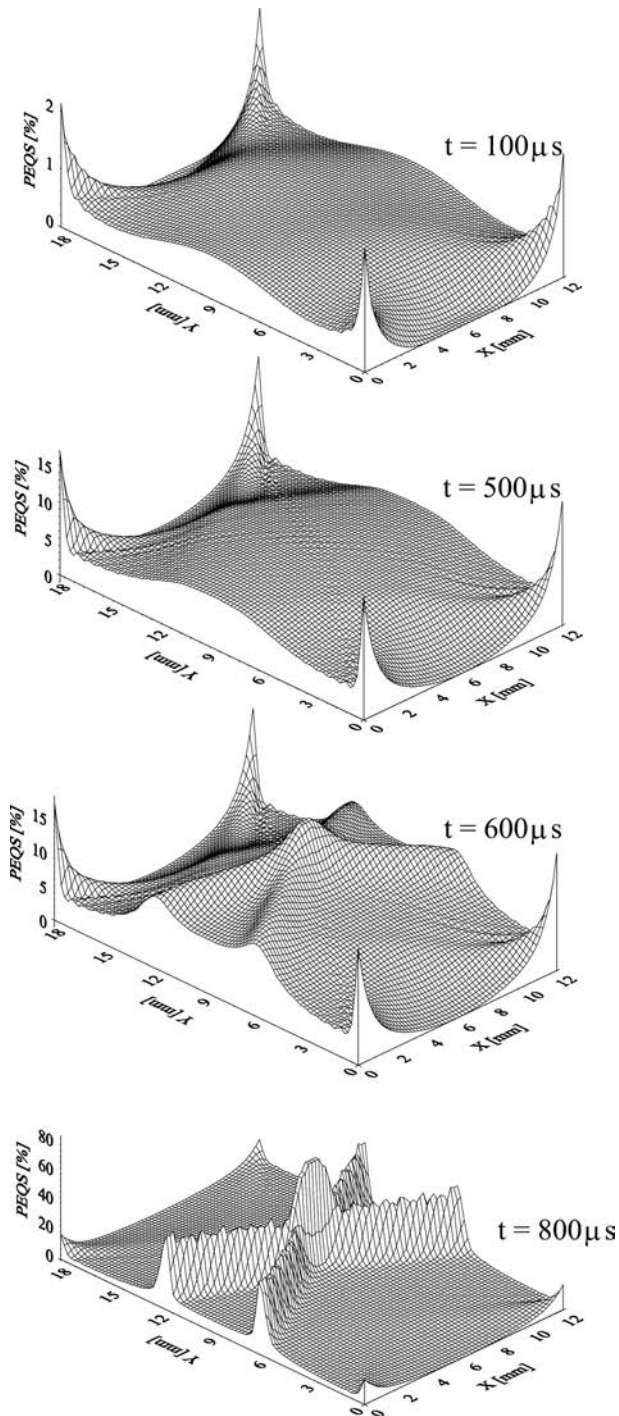


FIG. 16. Distributions of the equivalent plastic strain in a thin plate for chosen instants of the deformation process.

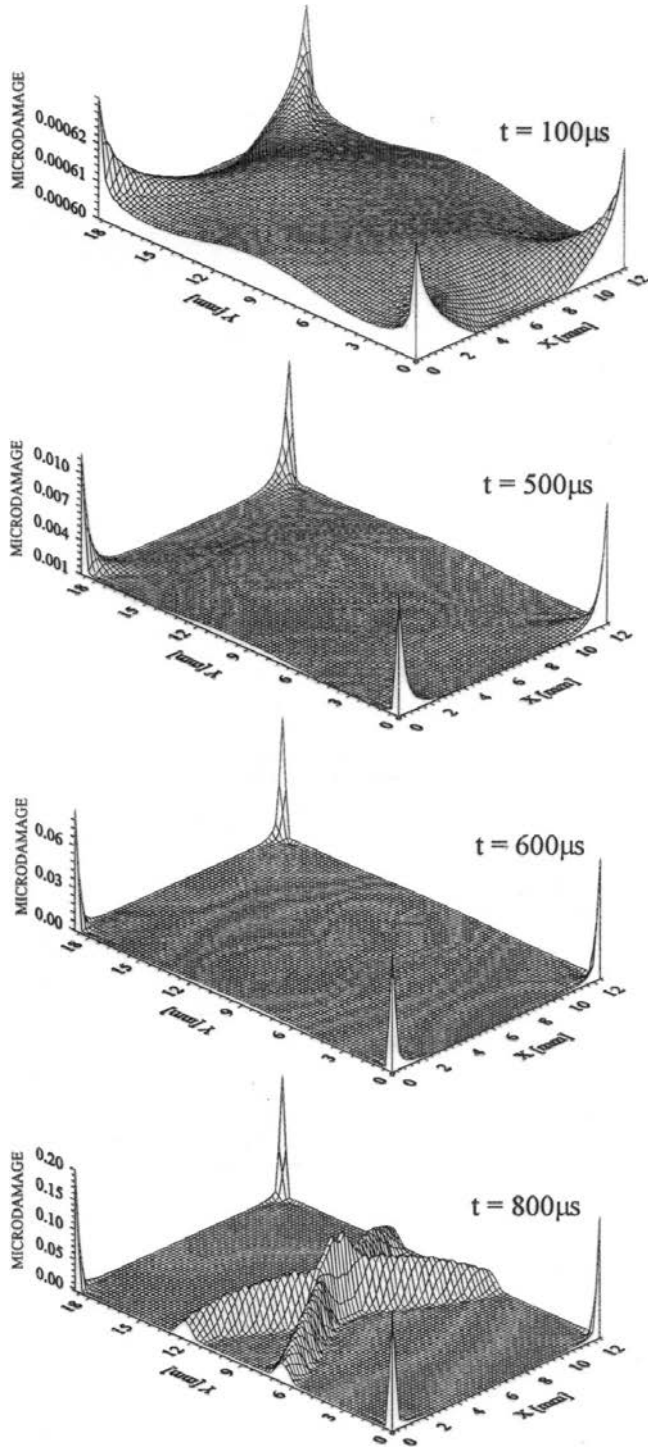


FIG. 17. Distribution of the microdamage for chosen instants of the deformation process.

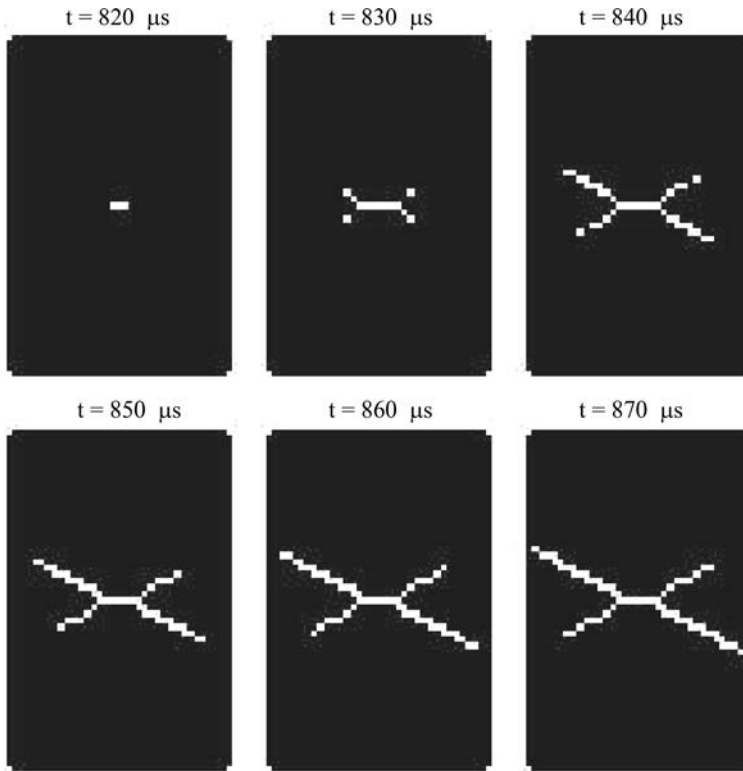


FIG. 18. Development of macrocracks in a thin plate.

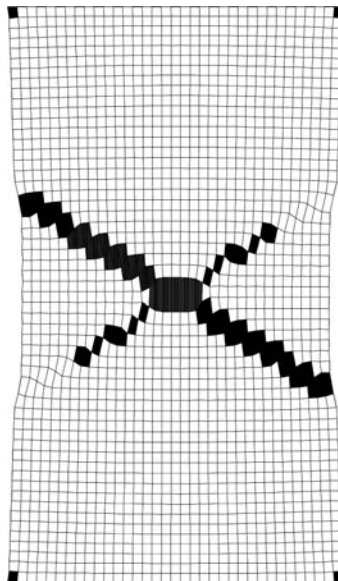


FIG. 19. Deformed configuration for final fracture of the plate.

to very small imperfections generated by numerical procedure. The obtained results are in accord with the experimental observations of CHAKRABARTI and SPRETNAK [2], cf. Fig. 20.

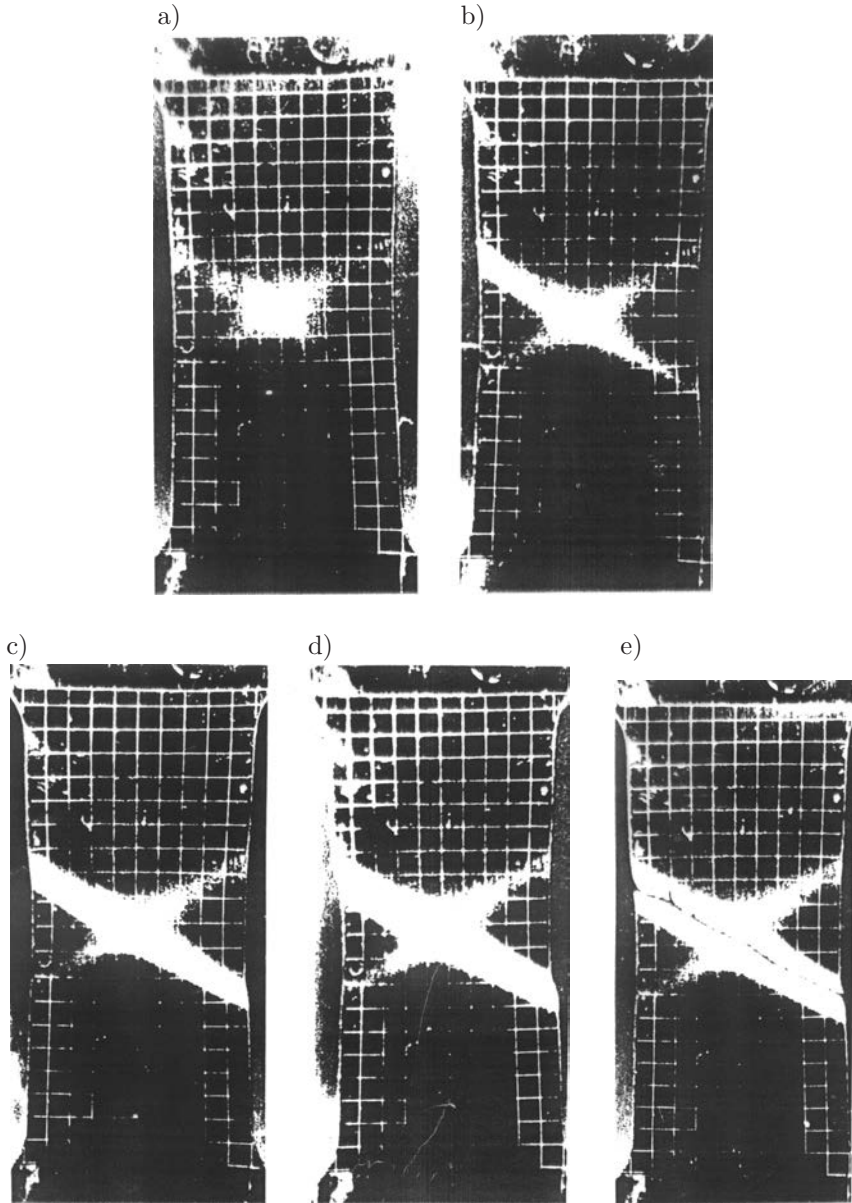


FIG. 20. Initiation and gradual development of instability bands in 0.099 cm thick specimen. One of the instability bands is getting predominant and much of the plastic deformation gets confined in this active band, cf. b)–d); failure takes place by shearing through the instability boundary of active instability band, cf. e) (after CHAKRABARTI and SPRETNAK [2]).

6. NUMERICAL EXAMPLE

6.1. Numerical solution of the initial boundary-value problem

We analyse the impact loaded plate with a pre-notched crack (Fig. 21). The material of the plate is assumed as a AISI 4340 steel and is modeled as elasto-viscoplastic with isotropic hardening-softening effects. We assume that the material softening is caused by intrinsic microdamage mechanism and thermomechanical coupling effect. The height of the specimen is equal to 200 mm, width is 100 mm and length of the initial crack (notch) is equal to 50 mm and is situated unsymmetrically, i.e., 110 mm from the bottom. The plane stress state is considered. As it is shown in Fig. 21, this specimen is loaded asymmetrically to the notch axis. The initial boundary value problem is different than those considered previously by DORNOWSKI and PERZYNA [13] and LI *et al.* [27].

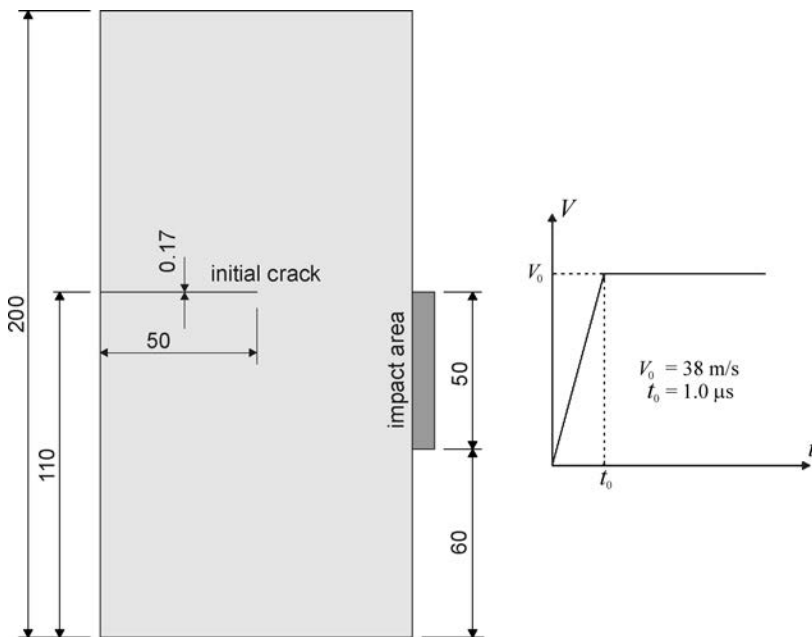


FIG. 21. The impact loaded plate with a prenotched crack.

To obtain the solution of the initial-boundary value problem formulated the finite difference method for regularized elasto-viscoplastic model is used⁶⁾. The

⁶⁾Numerical modelling of localized fracture phenomena in inelastic solids in dynamic loading processes by means of finite element method has been presented by ŁODYGOWSKI and PERZYNA [28].

loading condition is modeled by the velocity of nodes lying on the edge section with length equals to 50 mm, according to the relation

$$(6.1) \quad V(t) = V_0 t / t_0 \quad \text{for } t \leq t_0 \quad \text{and} \quad V(t) = V_0 \quad \text{for } t > t_0.$$

The rise time t_0 is fixed at 1.0 μs and the speed impact $V_0 = 38$ m/s. Initial conditions of the problem are homogeneous. In the discussion of the numerical results attention is focused mostly on the phenomenon of crack propagation.

The finite difference method with the explicit time integration scheme (conditionally stable) is used. The stress state in a nodal environment is determined by the iterative procedure of solving the dynamical yield condition with respect to the norm of the plastic deformation rate tensor. The elaborated algorithm satisfies the material objectivity principle with respect to diffeomorphism (any motion). We assume a nonuniform mesh of nodes which contain 180 000 nodes. The smallest mesh has the dimensions $\Delta\chi^1 = \Delta\chi^2 = 40$ μm , the time increment $\Delta t = 0.00356$ μs .

Figure 22 shows the Mises stress contour in the failure region following the impact. It can be clearly observed that the crack follow the path of the greatest Mises stress (the white band). The crack path changes its direction and has irregular (ragged) edges.

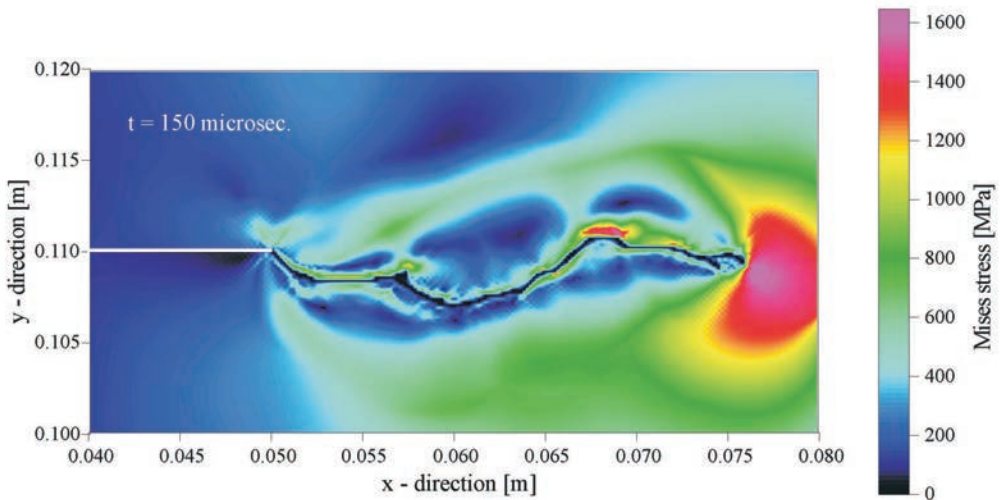


FIG. 22. Mises stress contours in the failure region.

In Fig. 23 the equivalent plastic strain distribution is displayed. It shows that there is a strain concentration region right in the front of the pre-notch tip. Along with the shear band progress the equivalent plastic strain intensity decreases. It confirms that the shear band transforms into an opening crack.

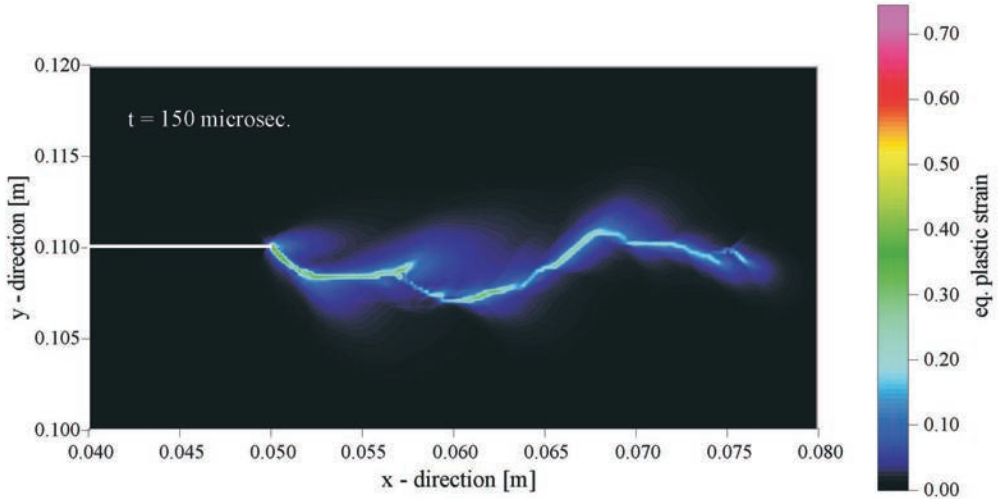


FIG. 23. Evolution of the equivalent plastic deformation in the fracture region.

The evolution of temperature is shown in Fig. 24. Zones of increased temperature correspond to the plastic zones. The maximum value of temperature is $\vartheta_{\max} = 750$ K. The effect of such a strong heating of the material results from its mechanical properties, i.e. the high strength steel, $R_m = 2000$ MPa. From Fig. 24 one may see that the computed temperature distribution is very heterogeneous. The similar effect has been noticed in experimental observations by GUDURU, ROSAKIS and RAVICHANDRAN [21].

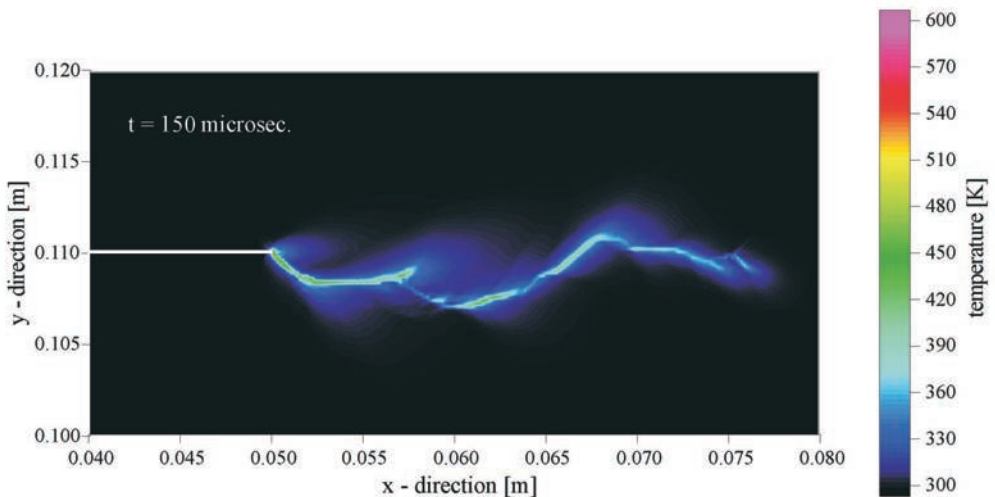


FIG. 24. Evolution of temperature in the fracture region.

In Fig. 25 the evolution of microdamage is presented. It can be clearly observed that the crack path (a black line) is very irregular and it widens steadily.

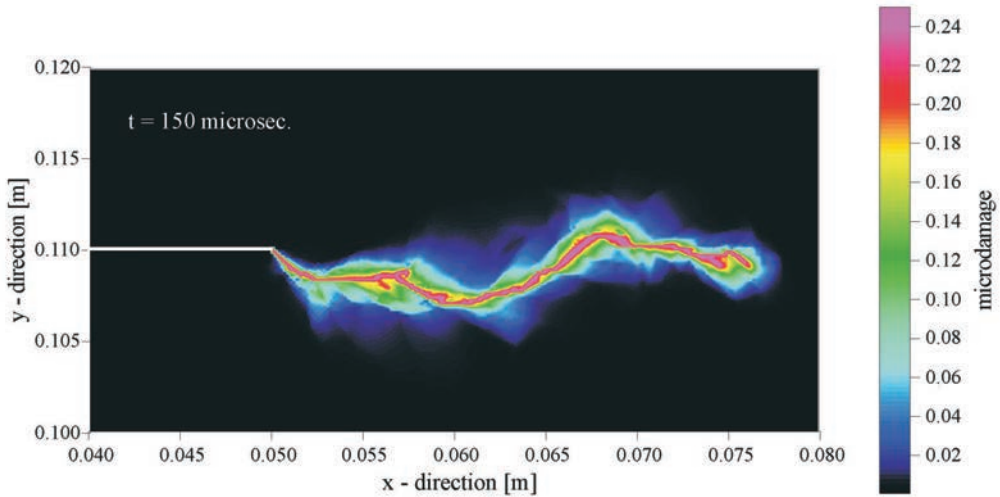


FIG. 25. Evolution of the microdamage and the crack path in the fracture region.

6.2. Discussion of the numerical results

From Fig. 22 we can observed that the macrocrack follows the path of the maximum value of the Mises stress $\tau_M = \left(\frac{2}{3}\boldsymbol{\tau}' : \boldsymbol{\tau}'\right)^{1/2}$. The macrocrack path changes its direction and has irregular edges. It results from the dispersive stress wave interaction and reflection of the considered impact adiabatic process as well as from the fact that the shear band transforms into an opening macrocrack, cf. GLEMA, ŁODYGOWSKI and PERZYNA [17–19]. The dissipation effect due to viscoplastic flow phenomena is observed in Fig. 23 as decay of the equivalent viscoplastic deformation intensity along with the shear band progress.

From Fig. 24 one may see that the computed temperature distribution along a propagating shear band is very heterogeneous and nonuniform. A similar effect has been noticed in experimental observations by GUDURU, ROSAKIS and RAVICHANDRAN [21]. They consistently observed, in all experiments where a propagating shear band was imaged, that the temperature distribution along the shear band is highly non-uniform, with discrete regions of high temperature, that look like “hot spots”. These hot spots are also seen to translate along the length of the shear band. Figure 26 shows one such image where the hot spots can be identified easily. This observation raises question about the spatial and temporal nature of shear deformation inside a shear band. We suggest that the

reason of this phenomenon is caused by interaction and reflection of dispersive stress waves during observed impact adiabatic process.

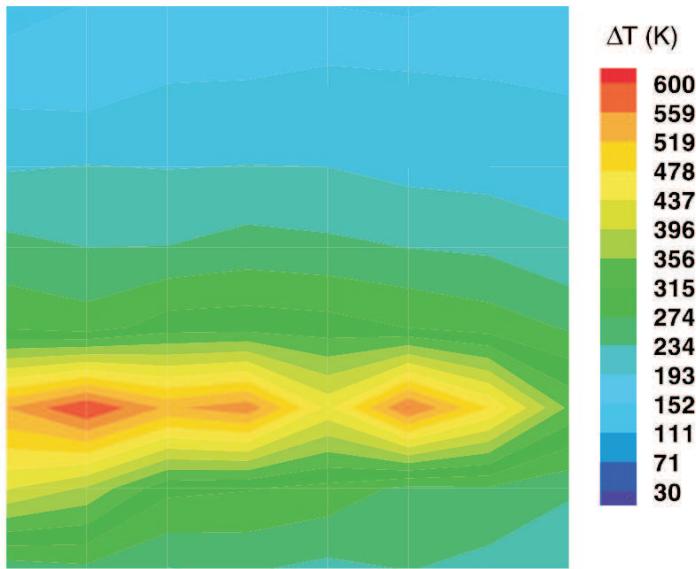


FIG. 26. A thermal image of a shear band showing non-uniform temperature distribution along the length of the band. After GUDURU, ROSAKIS and RAVICHANDRAN [21].

In our recent paper GLEMA, ŁODYGOWSKI and PERZYNA [20] investigated this problem numerically by using the finite element method and ABAQUS system. We used regularized thermo-elasto-viscoplastic constitutive model with one scalar internal state variable, namely equivalent inelastic deformation. We considered the initial boundary value problem, cf. Fig. 27, which is idealization of the process observed experimentally by GUDURU, ROSAKIS and RAVICHANDRAN [21], by assuming the velocity boundary condition and different material of the specimen (HY-100 steel). To identify the material functions and constants we used the experimental observation results obtained by CHO, CHI and DUFFY [4], cf. also CHI *et al.* [3]. The contour plots of equivalent inelastic deformation and temperature obtained for time instants 40, 50, 60 μs are visualized in Fig. 28 for unsymmetric impact. To show better that we obtained non-uniform temperature distribution along the shear band we present the magnification of the result for the field of temperature at 60 μs in Fig. 29. The function of shear band length and propagation velocity of its front were also calculated, cf. Fig. 30. The advances of shear band length in experimental observations and in numerical computations have similar find values and the functions presenting its evolution are comparable. The comparison of the shear band propagation velocity reaches the same conclusion.

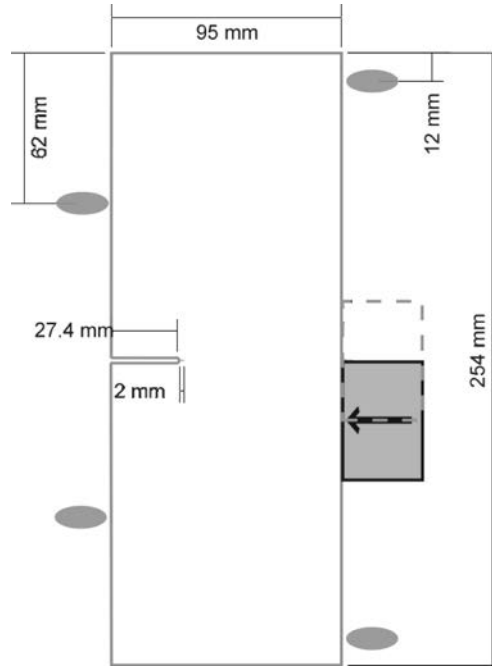
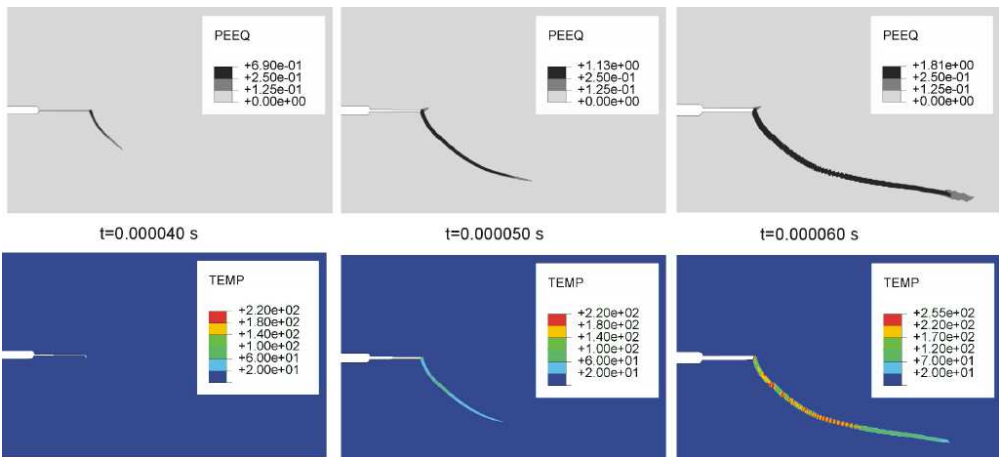


FIG. 27. Specimen geometry.

FIG. 28. Evolution of plastic equivalent deformation and temperature along the shear band for unsymmetric impact (for 40, 50, 60 μ s).

Rather the qualitative agreement is verified, than strict comparison of values. The common sudden velocity drop, observed in experiment and simulations, is specially worth to point it out.

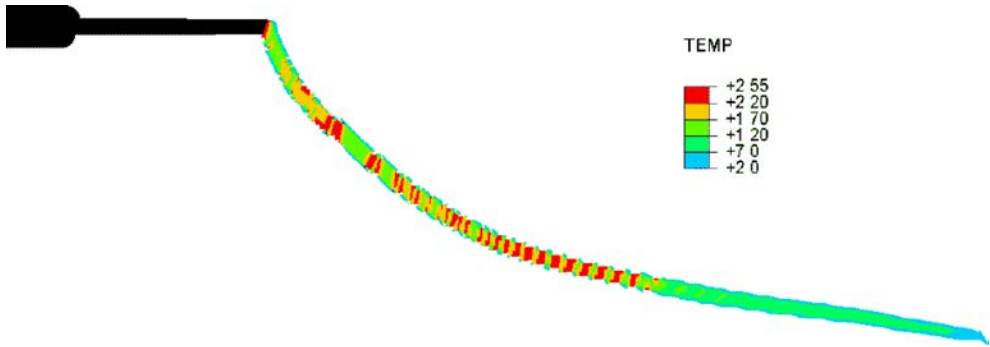


FIG. 29. Magnification of the results for the field of temperature at $60 \mu\text{s}$ for unsymmetric impact.

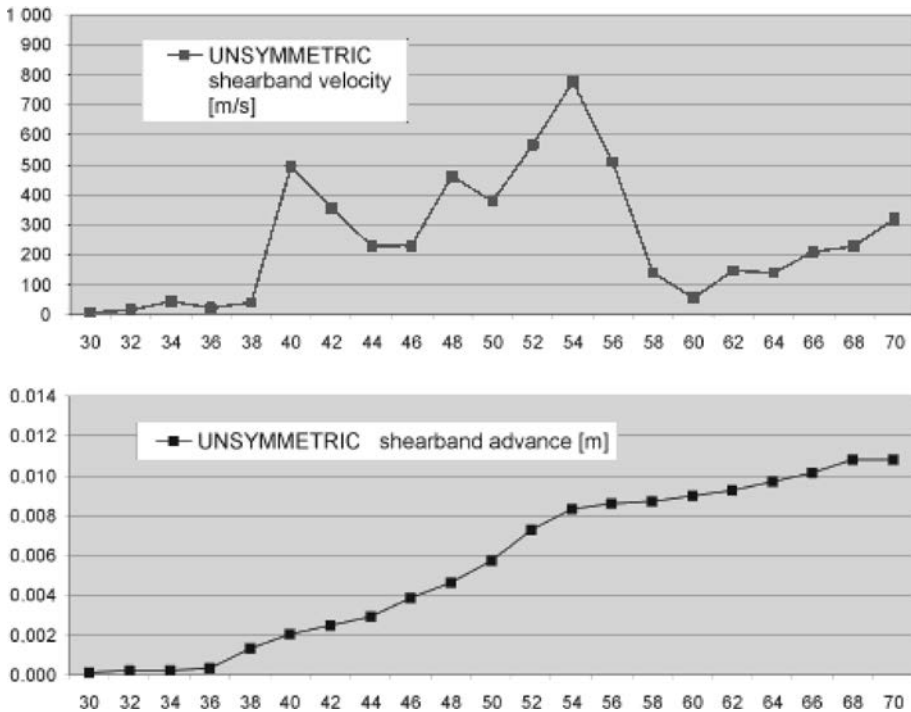


FIG. 30. Propagation velocity of shear band front and shear band length as functions of time, for unsymmetric impacts.

The remark concerning the temperature distribution goes in the same direction. There is valuable to expose that numerical results show the particular character of experimental ones, with occurrence of discrete regions of high temperature, that are described as “hot spots”, cf. Fig. 29. Appearance of several local extremes take place after the mentioned above drop of propagation ve-

locity of the shear band tip. The evolution of described variables suggests the step-wise nature of shear band propagation phenomena caused by the reflection and interaction of dispersive stress waves during impact adiabatic process.

From the results presented in Figs. 22–25 one can easily observe that the localized fracture is preceded by the propagation of the shear band⁷⁾. This is also visible in Fig. 25, where the propagated localized region of critical microdamage (it means the fracture front for $\xi = \xi^F$) is preceded by the shear band along which the microdamage is smaller than $\xi = \xi^F$. The evolution of the microdamage and the macrocrack path in the fracture region shown in Fig. 25 indicates that the macrocrack path is very irregular and it widens steadily. It seems that in some places of the macrocrack we can expect the branching effect as it has been observed by GUDURU, ROSAKIS and RAVICHANDRAN [21], cf. Fig. 8.

Of course, we have to take into account that during experimental observations they investigated real material (C300 steel), which can have some impurities, which help to generate the shear band bifurcation, while we assumed fully homogeneous material of the plate for our numerical simulation.

We can conclude that the shear band branching can be generated by reflection and interaction of dispersive stress waves during adiabatic impact process and by some real existing impurities of the investigated material.

7. EPILOGUE

The elaborated numerical algorithm satisfies the material objectivity principle with respect to diffeomorphism (any motion). The discretization parameters are assumed in such a way that the problem of mesomechanics is solved properly. A thin shear band region of finite width which undergoes significant deformation and temperature rise has been determined. Its evolution until occurrence of final fracture has been simulated. Shear band advance, as a function of time and the evolution of the Mises stress, equivalent plastic deformation, temperature and the macrocrack path in the fracture region have been determined. Qualitative comparison of numerical results with experimental observation data has been presented. Based on this comparison we can conclude that our numerical results are in accord with the experimental observations performed by GUDURU, ROSAKIS and RAVICHANDRAN [21]. Particularly, in our numerical simulation the temperature evolution along the shear band region is very nonuniform and the obtained macrocrack path is very irregular and is showing a tendency to branching phenomenon similarly as have been suggested by experimental observations. The numerical results obtained have been proven the usefulness of

⁷⁾For a thorough discussion of numerical investigation of propagation of shear bands in inelastic solids please consult GLEMA, ŁODYGOWSKI and PERZYNA [20].

the thermo-elasto-viscoplastic theory in the numerical investigation of dynamic shear band propagation and localized fracture phenomena.

ACKNOWLEDGMENT

The paper was prepared within the framework of the Research Projects N N501 036435 and N N519 419435 of the Ministry of Higher Education and Science of Poland.

REFERENCES

1. R. ABRAHAM, J. E. MARSDEN, T. RATIU, *Manifolds, Tensor Analysis and Applications*, Springer, Berlin, 1988.
2. A. K. CHAKRABARTI, J. W. SPRETNAK, *Instability of plastic flow in the direction of pure shear*, Metallurgical Transactions, **6A**, 733–747, 1975.
3. Y. C. CHI, S. H. LEE, K. CHO, J. DUFFY, *The effects of tempering and test temperatures on the dynamic fracture initiation behaviour of an AISI 4340 VAR steel*, Brown University Technical Report, August 1988.
4. K. CHO, Y. C. CHI, J. DUFFY, *Microscopic observations of adiabatic shear bands in three different steels*, Brown University Report No DAAL03-88-K-0015/3, September 1988.
5. B. D. COLEMAN, W. NOLL, *The thermodynamics of elastic materials with heat conduction and viscosity*, Arch. Rational Mech. Anal., **13**, 167–178, 1963.
6. R. COURANT, K. O. FRIEDRICHS, H. LEWY, *Über die Partiellen Differenzgleichungen der Mathematischen Physik*, Math. Ann., **100**, 32–74, 1928.
7. D. R. CURRAN, L. SEAMAN, D. A. SHOCKEY, *Dynamic failure of solids*, Physics Reports, **147**, 253–388, 1987.
8. R. DAUTRAY, J. L. LIONS, *Mathematical Analysis and Numerical Methods for Science and Technology*, Vol. 6. Evolution Problems II, Springer, Berlin 1993.
9. W. DORNOWSKI, *Influence of finite deformation on the growth mechanism of microvoids contained in structural metals*, Arch. Mech., **51**, 71–86, 1999.
10. W. DORNOWSKI, P. PERZYNA, *Constitutive modelling of inelastic solids for plastic flow processes under cyclic dynamic loadings*, In: Transaction of the ASME, J. Eng. Materials and Technology, **121**, 210–220, 1999.
11. W. DORNOWSKI, P. PERZYNA, *Localization phenomena in thermo-viscoplastic flow processes under cyclic dynamic loadings*, CAMES, **7**, 117–160, 2000.
12. W. DORNOWSKI, P. PERZYNA, *Localized fracture phenomena in thermo-viscoplastic flow processes under cyclic dynamic loadings*, Acta Mechanica, **155**, 233–255, 2002.
13. W. DORNOWSKI, P. PERZYNA, *Numerical investigation of localized fracture phenomena in inelastic solids*, Foundations of Civil and Environmental Engineering, **7**, 79–116, 2006.
14. M. K. DUSZEK, P. PERZYNA, *The localization of plastic deformation in thermoplastic solids*, Int. J. Solids Structures, **27**, 1419–1443, 1991.

15. M. K. DUSZEK–PERZYNA, P. PERZYNA, *Analysis of the influence of different effects on criteria for adiabatic shear band localization in inelastic solids* [in:] Proceedings Material Instabilities: Theory and Applications, ASME Congress, Chicago, 9–11 November 1994, R. C. BATRA and H. M. ZBIB [Eds.], AMD-Vol. 183/MD-Vol.50, ASME, New York, pp. 59–85, 1994.
16. D. R. DURRAN, *Numerical Methods for Wave Equations in Geophysical Fluid Dynamics*, Springer, New York, 1999.
17. A. GLEMA, T. ŁODYGOWSKI, P. PERZYNA, *Interaction of deformation waves and localization phenomenon in inelastic solids*, Comput. Methods Appl. Mech. Engng., **183**, 123–140, 2000.
18. A. GLEMA, T. ŁODYGOWSKI, P. PERZYNA, *The role of dispersion for the description of strain localization in materials under impact loading*, [in:] European Conference on Computational Mechanics, June 26–29, 2001, Cracow, Poland.
19. A. GLEMA, T. ŁODYGOWSKI, P. PERZYNA, *Localization of plastic deformations as a result of wave interaction*, CAMES, **10**, 81–91, 2003.
20. A. GLEMA, T. ŁODYGOWSKI, P. PERZYNA, *Numerical investigation of dynamic shear bands in inelastic solids as a problem of mesomechanics*, Comput. Mech., **41**, 219–229, 2008.
21. P. R. GUDURU, A. J. ROSAKIS, G. RAVICHANDRAN, *Dynamic shear bands: an investigation using high speed optical and infrared diagnostic*, Mechanics of Materials, **33**, 371–402, 2001.
22. P. R. GUDURU, A. T. ZEHNDER, A. J. ROSAKIS, G. RAVICHANDRAN, *Dynamic full field measurements of crack tip temperatures*, Engineering Fracture Mechanics, **68**, 1535–1556, 2001.
23. B. GUSTAFSSON, H. O. KREISS, J. OLIGER, *Time Dependent Problems and Difference Methods*, John Wiley, New York, 1995.
24. J. W. HUTCHINSON, *Plasticity at the micron scale*, Int. J. Solids and Structures, **37**, 225–238, 2000.
25. I. R. IONESCU, M. SOFONEA, *Functional and Numerical Methods in Viscoplasticity*, Oxford 1993.
26. J. N. JOHNSON, *Dynamic fracture and spallation in ductile solids*, J. Appl. Phys., **52**, 2812–2825, 1981.
27. S. LI, W.-K. LIU, D. QIAN, P. R. GUDURU, A. J. ROSAKIS, *Dynamic shear band propagation and micro-structure of adiabatic shear band*, Comput. Methods Appl. Mech. Engng., **191**, 73–92, 2001.
28. T. ŁODYGOWSKI, P. PERZYNA, *Numerical modelling of localized fracture of inelastic solids in dynamic loading processes*, Int. J. Num. Meth. Engng., **40**, 4137–4158, 1997.
29. J. E. MARSDEN, T. J. R. HUGHES, *Mathematical Foundations of Elasticity*, Prentice-Hall, Englewood Cliffs, New York, 1983.
30. H. C. MEYERS, *Dynamic Behaviour of Materials*, John Wiley, New York 1994.
31. A. NEEDLEMAN, *Computational mechanics at the mesoscale*, Acta Materialia, **48**, 105–124, 2000.

32. J. A. NEMES, J. EFTIS, *Constitutive modelling of the dynamic fracture of smooth tensile bars*, Int. J. Plasticity, **9**, 243–270, 1993.
33. J. OLDROYD, *On the formulation of rheological equations of state*, Proc. Roy. Soc. (London), **A 200**, 523–541, 1950.
34. P. PERZYNA, *The constitutive equations for rate sensitive plastic materials*, Quart. Appl. Math., **20**, 321–332, 1963.
35. P. PERZYNA, *Fundamental problems in viscoplasticity*, Advances in Applied Mechanics, **9**, 243–377, 1966.
36. P. PERZYNA, *Thermodynamic theory of viscoplasticity*, Advances in Applied Mechanics, **11**, 313–354, 1971.
37. P. PERZYNA, *Constitutive modelling of dissipative solids for postcritical behaviour and fracture*, ASME J. Eng. Materials and Technology, **106**, 410–419, 1984.
38. P. PERZYNA, *Internal state variable description of dynamic fracture of ductile solids*, Int. J. Solids Structures, **22**, 797–818, 1986a.
39. P. PERZYNA, *Constitutive modelling for brittle dynamic fracture in dissipative solids*, Arch. Mechanics, **38**, 725–738, 1986b.
40. P. PERZYNA, *Instability phenomena and adiabatic shear band localization in thermoplastic flow processes*, Acta Mechanica, **106**, 173–205, 1994.
41. P. PERZYNA, *Interactions of elastic-viscoplastic waves and localization phenomena in solids*, [in:] Proceedings IUTAM Symposium on Nonlinear Waves in Solids, August 15–20, 1993, Victoria, Canada, J. L. WEGNER and F. R. NORWOOD [Eds.], ASME 1995, pp. 114–121, 1995.
42. P. PERZYNA, *Thermo-elasto-viscoplasticity and damage*, [in:] Handbook of Materials Behaviour Models, J. LEMAITRE [Ed.], Academic Press, New York, pp. 821–834, 2001.
43. P. PERZYNA, *The thermodynamical theory of elasto-viscoplasticity*, Engineering Transactions, **53**, 235–316, 2005.
44. P. PERZYNA, *Application of the thermodynamical theory of elasto-viscoplasticity in modern manufacturing processes*, [in:] Damage Mechanics and Micromechanics of Localized Fracture Phenomena in Inelastic Solids, CISM Courses and Lectures, G. Z. VOYIADJIS [Ed.], Vol. **525**, Springer, Wien New York, pp. 225–376, 2011.
45. P. PERZYNA, A. DRABIK, *Description of micro-damage process by porosity parameter for nonlinear viscoplasticity*, Arch. Mech., **41**, 895–908, 1989.
46. R. D. RICHTMYER, *Principles of Advance Mathematical Physics*, Vol. I, Springer, New York 1978.
47. R. D. RICHTMYER, K. W. MORTON, *Difference Methods for Initial-Value Problems*, John Wiley, New York 1967.
48. S. SHIMA, M. OYANE, *Plasticity for porous solids*, Int. J. Mech. Sci., **18**, 285–291, 1976.
49. D. A. SHOCKEY, L. SEAMAN, D. R. CURRAN, *The microstatistical fracture mechanics approach to dynamic fracture problem*, Int. J. Fracture, **27**, 145–157, 1985.
50. D. SIDEY, L. F. COFFIN, *Low-cycle fatigue damage mechemism at high temperature*, [in:] Fatigue Mechanism, Proc. ASTM STP 675 Symposium, Kansas City, Mo., May 1978, J. T. FONG [Ed.], Baltimore, pp. 528–568, 1979.

51. L. J. SLUYS, *Wave propagation, localization and dispersion in softening solids*, Doctoral thesis, Delft University Press, Delft, 1992.
52. G. STRANG, G. J. FIX, *An Analysis of the Finite Element Method*, Prentice-Hall, Englewood Cliffs 1973.
53. S. A. THAU, *Linear dispersive waves*, [in:] *Nonlinear Waves*, S. LEIBOVICH and A. R. SEEBASS [Eds.], Cornell University Press, Ithaca, 1974, pp. 44-81.
54. C. TRUESDELL, W. NOLL, *The nonlinear field theories*, *Handbuch der Physik*, Band III/3, pp. 1-579, Springer, Berlin, 1965.
55. G. B. WHITHAM, *Linear and Nonlinear Waves*, John Wiley, New York, 1974a.
56. G. B. WHITHAM, *Dispersive waves and variational principles*, [in:] *Nonlinear Waves*, S. LEIBOVICH and A. R. SEEBASS [Eds.], Cornell University Press, Ithaca, 1974b, pp. 139-169.
57. M. ZHOU, A. J. ROSAKIS, G. RAVICHANDRAN, *Dynamic propagating shear band in impact-loaded prenotched plates. I. Experimental investigations of temperature signatures and propagation speed*, *J. Mech. Phys. Solids*, **44**, 981-1006, 1996.
58. M. ZHOU, G. RAVICHANDRAN, A. J. ROSAKIS, *Dynamic propagating shear band in impact-loaded prenotched plates. II. Numerical simulations*, *J. Mech. Phys. Solids*, **44**, 1007-1032, 1996.

Received July 18, 2011.
